# Can a Formally Zwitterionic Rhodium(I) Complex Emulate the Charge Density of a Cationic Rhodium(I) Complex? A Combined Synchrotron X-ray and Theoretical Charge-Density Study

El-Eulmi Bendeif, Chérif F Matta, Mark Stradiotto, Pierre Fertey, Claude Lecomte

El-Eulmi Bendeif, Chérif F Matta, Mark Stradiotto, Pierre Fertey, Claude Lecomte. Can a Formally Zwitterionic Rhodium(I) Complex Emulate the Charge Density of a Cationic Rhodium(I) Complex? A Combined Synchrotron X-ray and Theoretical Charge-Density Study. Inorganic Chemistry, 2012, 51 (6), pp.3754-3769. 10.1021/ic2026347 . hal-04398334

# Can a Formally Zwitterionic Rhodium(I) Complex Emulate the Charge Density of a Cationic Rhodium(I) Complex? A Combined Synchrotron X-Ray and Theoretical Charge Density Study

| | |
|---|---|
| Journal: | *Inorganic Chemistry* |
| Manuscript ID: | ic-2011-026347.R2 |
| Manuscript Type: | Article |
| Date Submitted by the Author: | n/a |
| Complete List of Authors: | Bendeif, El-Eulmi; Nancy universite , crystallography<br>Matta, Cherif; Mount Saint Vincent University, Department of Chemistry and Physics<br>Stradiotto, Mark; Dalhousie University,<br>Fertey, Pierre; Syncrotron Solei,<br>Lecomte, C; Nancy universite , crystallography |
| | |

# Can a Formally Zwitterionic Rhodium(I) Complex Emulate the Charge Density of a Cationic Rhodium(I) Complex? A Combined Synchrotron X-Ray and Theoretical Charge Density Study[1]

El-Eulmi Bendeif,(1,2) Chérif F. Matta,(1,3,4)* Mark Stradiotto,(4) Pierre Fertey,(2) Claude Lecomte(1)*

*(1) Laboratoire de Cristallographie, Résonance Magnétique et Modélisation CRM2, UMR CNRS 7036, Institut Jean Barriol, Faculté des Sciences et Technologies, Université de Lorraine, BP 70239, 54506 Vandoeuvre-les-Nancy, France.*
*(2) Synchrotron Soleil - L'Orme des Merisiers Saint-Aubin - BP 48 91192 Gif-sur-Yvette, France.*
*(3) Department of Chemistry and Physics, Mount Saint Vincent University, Halifax, Nova Scotia, Canada B3M 2J6.*
*(4) Department of Chemistry, Dalhousie University, Halifax, Nova Scotia, Canada B3H 4J3.*

***Running title head*: Cationic and Zwitterionic Rh Complexes**

## SYNOPSIS

Low temperature synchrotron X-ray diffraction and high level of theoretical calculations were used to determine accurate electron density distributions of two structurally related cationic ([($\kappa^2$-3-$P^i$Pr$_2$-2-$N$Me$_2$-indene)Rh(COD)](CF$_3$SO$_3$), [**1c**](CF$_3$SO$_3$)), and formally zwitterionic ([($\kappa^2$-3-$P^i$Pr$_2$-2-$N$Me$_2$-indenide)Rh(COD)], **1z**) complexes, (COD = $\eta^4$-1,5-cyclooctadiene). Both experiment and theory show a striking similarity of charge distribution and of the molecular electrostatic potential, $V$(**r**), in the region of the Rh catalytic center. These observations confirm, for the first time, that appropriately designed zwitterionic complexes can effectively emulate the charge distribution found within cationic platinum-group metal catalyst complexes, in keeping with recent catalytic investigations.

---

[1] This paper is dedicated to the memory of Professor Richard F. W. Bader (1931-2012) the pioneer who has developed the quantum theory of atoms in molecules (QTAIM) and of the topological analysis of molecular scalar and vector fields.

# ABSTRACT

The molecular electron densities of structurally related cationic ([(κ$^2$-3-$P^i$Pr$_2$-2-$N$Me$_2$-indene)Rh(COD)](CF$_3$SO$_3$), [**1c**](CF$_3$SO$_3$)), and formally zwitterionic ([(κ$^2$-3-$P^i$Pr$_2$-2-$N$Me$_2$-indenide)Rh(COD)], **1z**) complexes were accurately determined using synchrotron bright source X-ray radiation at 30K followed by multipolar refinement (COD = η$^4$-1,5-cyclooctadiene). The densities were also obtained from density functional theory (DFT) calculations with a large, locally dense, basis set. A 28 electron ([Ar]3$d^{10}$) core of the Rh atom was modeled by an effective core potential to obtain a density which was then augmented with relativistic cores according to the Keith-Frisch approximation. Calculations were performed at the experimental geometry and a after vacuum-phase geometry optimization starting from the experimental geometry. Experimental and calculated geometries and electron density distributions show that the electron density and the electronic structure in the region of the Rh center is not significantly altered by the protonation of the aromatic ring, and that formal removal of CF$_3$SO$_3$H from [**1c**](CF$_3$SO$_3$) affords a complex **1z** possessing substantial zwitterionic character (with a charge separation of *ca.* 0.9 electronic charge) featuring a negatively charged aromatic indenide framework. Further, the molecular electrostatic potentials of **1c** and **1z** exhibit a similar topography around the metal, despite being drastically different in the vicinity of the indene or indenide portion of the cation (**1c**) and zwitterion (**1z**), respectively. Collectively, these observations obtained from high-level experimental and theoretical electron density analysis confirm, for the first time, that appropriately designed zwitterionic complexes can effectively emulate the charge distribution found within ubiquitous cationic platinum-group metal catalyst complexes, in keeping with recent catalytic investigations.

# 1. INTRODUCTION

Cationic platinum-group metal complexes (*i.e.*, $[L_nM]^+X^-$) figure prominently in modern organometallic chemistry research, owing to the ability of such species to mediate challenging substrate transformations in a manner that in some cases cannot be achieved by the use of simple neutral complexes.[1-5] Although the study of cationic platinum-group metal complexes continues to enable breakthroughs in metal-mediated transformations, incompatibility with low- and high-polarity solvents can limit the effective operational scope of such salts.[3,6] Furthermore, the design of reactive cationic complexes is complicated by the fact that the outer-sphere counteranion ($X^-$) can influence profoundly the behavior of the complex via ion pairing, often in a manner that cannot be predicted easily.[7,8]

In an effort to combine the desirable reactivity properties of cationic species with the broad solvent tolerance of neutral complexes, the rational design of formally zwitterionic platinum-group metal complexes has garnered widespread attention within the field of organometallic chemistry.[9] While formal atom charges (*e.g.*, on the basis of Lewis representations) do not represent true charges within a complex, it is plausible to envision that a zwitterionic motif which effectively emulates the charge distribution featured in a cationic complex might indeed be established if formal charge separation between the ancillary ligand and the coordinated cationic platinum-group metal fragment can be achieved. Several unique classes of formally zwitterionic platinum-group metal species that appear to meet such design criteria have emerged, owing to recent advances in ancillary ligand design.[9] Notably, comparative reactivity studies of structurally related cationic and zwitterionic platinum-group metal species reveal that the reactivity of such zwitterions is in many instances reminiscent of, and in some cases superior to,[10-12] related cationic complexes.[9] Notwithstanding these recent synthetic and reactivity advances, no comprehensive experimental/computational analysis comparing the charge density within structurally analogous cationic and zwitterionic platinum-group metal complexes has appeared in the literature. Such investigations are critically needed in order to gain a better understanding of the electron distribution in conventional cationic platinum-group metal species, as well as to quantify the extent to which charge separation exists within a given zwitterionic framework.

Herein we report the first low temperature (30(1) K) synchrotron crystallographic study of the electron density[13,14] combined with a theoretical analysis of the topology of the electron density within two structurally analogous cationic and zwitterionic platinum-group metal complexes. The analysis of the electron density is based on the quantum theory of atoms in molecules (QTAIM).[15-17]

Overarching goals of this study include: (a) Evaluating the extent to which commonly invoked organometallic bonding formalisms can represent experimentally observed/computationally predicted electron density distributions; and (b) assessing the capacity of a formally zwitterionic platinum-group metal complex to emulate the charge distribution featured within a structurally analogous cationic complex via formal charge separation. The cationic and zwitterionic complexes selected for this study are derived from 3-$P^{i}Pr_2$-2-$NMe_2$-indene (**Chart 1**); both the cation [($\kappa^2$-3-*P*$^{i}$$Pr_2$-2-*N*$Me_2$-indene)Rh(COD)]($CF_3SO_3$) ([**1c**]($CF_3SO_3$)) and the zwitterionic species [($\kappa^2$-3-*P*$^{i}$$Pr_2$-2-*N*$Me_2$-indenide)Rh(COD)] (**1z**) have proven useful in a range of catalytic applications involving σ-bond activation (COD = $\eta^4$-1,5-cyclooctadiene).[18,19] In contrast to conventional $\eta^5$-indenyl species,[20-25] platinum-group metal zwitterions such as **1z** can be viewed as comprising a formally cationic metal fragment (*i.e.*, (COD)Rh$^+$ in **1z**) whose charge is counterbalanced by a sequestered, formally anionic, 10 π-electron indenide unit that is incorporated into the backbone of the associated κ$^2$-*P*,*N*-ligand. This paper demonstrates that this approach is, indeed, a viable one given the nearly identical charge distributions within the Rh coordination sphere of **1z** and **1c**.

## 2. SYNCHROTRON X-RAY CRYSTALLOGRAPHIC EXPERIMENT

### 2.1 X-Ray Diffraction Data Collection and Reduction

To investigate the charge density distribution of the cationic and zwitterionic Rh(I) species (**1c** and **1z**), accurate high resolution single-crystal X-ray diffraction experiments at 30(1) K were performed at the CRISTAL beamline at SOLEIL Synchrotron (Saint Aubin, France). Good quality single crystals of suitable size (typically 0.1 × 0.1 × 0.1 mm) were used for the data collection. They were fixed with silicon grease onto a short and thin microfabricated polyimide film attached to a solid non-magnetic stainless steel pin (MicroMounts, MiTeGen) to avoid any unsteady motion due to the He flow and mounted on the goniometer head of the high resolution Newport four-circle diffractometer equipped with an Oxford Atlas two-dimensional CCD detector (135 mm). To decrease thermal smearing effects, the samples were cooled from ambient temperature to 30(1) K over a period of 2 h using a Helium Cryoindustry cooling device. The temperature was calibrated beforehand using a K-type Chromel-Alumel thermocouple positioned at the same place on the crystal. The temperature stability was found to be within ±0.5 K during the duration of the measurements. It is worth noting that this is the first experiment at Synchrotron Soleil devoted to charge density modelling.

In order to ensure high redundancies, the intensity data were accurately collected using ω oscillation scans of 1° per frame repeated at eight different φ positions at 2θ of 0°, 40 ° and 70°. The low and high resolution reflections were measured with a radiation exposure time of 1 s and 3 s respectively. The shorter exposure times were used to accurately record the intense low-order data, avoiding pixel overflow or integration failure, while the high-angle sets utilized the longer exposure times to improve the measurements statistics. The sample-to-detector distance was 100 mm and the wavelengths of the radiation used were 0.54737 Å and 0.54856 Å for **1z** and [**1c**]($CF_3SO_3$) respectively. These short wavelengths (close to the K edge of Rh (λ=0.53428 Å)) were chosen in order to minimise the absorption effects. Five different data sets were collected: a low-angle data set, using no attenuator, was collected first; then the same data collection was performed with an attenuator factor of 4; then very low-angle strong reflections were measured using an attenuator factor of 30; finally, two high-angle data sets were collected with and without an attenuator.

X-ray data were integrated using the Crysalis-Red program.[26] The absorption was small (due to the choice of the radiation wavelengths), but the data were nevertheless corrected by an empirical absorption correction. The different sets of measured reflections were subsequently merged and scaled using SORTAV.[27] A total of 1 355 281 and 812 400 reflections intensities collected up to the maximum resolution of $\sin\theta_{max}/\lambda$ = 1.403 $Å^{-1}$ and 1.366 $Å^{-1}$ were merged into 57 136 and 42449 unique reflections for the cation ([**1c**]($CF_3SO_3$)) and the zwitterion (**1z**), respectively. Data were 98% complete to $\sin\theta/\lambda$ = 1.08 $Å^{-1}$, with all of the missing data above $\sin\theta/\lambda$ = 0.96 $Å^{-1}$. The internal agreement factors for all data are $R_{Int}(I)$ = 0.068 and 0.058 with an average redundancy of 24 and 19 for [**1c**]($CF_3SO_3$) and **1z**, respectively.

## 2.2 Spherical Atom Refinement

The structures of the cationic and zwitterionic complexes [**1c**]($CF_3SO_3$) and **1z** (**Figure 1**) were solved using direct methods (*SHELXS*97)[28,29] and refined by full-matrix least-squares on $F^2$ using the spherical-atom model (*SHELXL*97),[28,29] with no constraints applied. All of the calculations were carried out using the *WinGX* package of crystallographic programs.[30,31] All of the non-hydrogen atoms were allowed anisotropic thermal motion. All hydrogen atoms were located in Fourier difference maps and refined initially with isotropic thermal displacement parameters. The full experimental details and refinements results for [**1c**]($CF_3SO_3$) and **1z** are summarized in **Table 1.**

## 2.3 Multipolar Refinement and Electronic Properties Calculations

The multipole electron density model of Hansen and Coppens[32] as implemented in the program package MoPro[33,34] was used. It allows for modelling of the valence electron density using atom-centred multipole functions (**Equations 1 and 2**):

$$\rho_{\mathrm{atom}}(\vec{\mathrm{r}}) = \rho_{\mathrm{core}}(r) + P_{\mathrm{val}}\,\kappa^3\,\rho_{\mathrm{val}}^{\mathrm{sph}}(\kappa r) + \rho_{\mathrm{multipolar}}(\vec{\mathrm{r}}) \qquad (1)$$

where

$$\rho_{\mathrm{multipolar}}(\vec{\mathrm{r}}) = \sum_{l=0}^{l_{\max}} \kappa'^3 R_l(\kappa' r) \sum_{m=0}^{l} P_{lm\pm}\, Y_{lm\pm}(\theta,\varphi). \qquad (2)$$

As a starting point of the refinement the independent atom model (IAM) was used. The multipole refinement was undertaken using all positive unique reflections. Several models were tried, but the best results were obtained with a treatment that proceeded as follows. The multipole expansion was truncated at the hexadecapole level for all non-hydrogen atoms, while only bond-directed dipoles were applied for H atoms. The relativistic Dirac-Fock atomic wavefunctions[35,36] were used to describe both the core and the valence-electron shells. The electronic configuration ($5s^1 4d^8$) was used for rhodium with the $5s^1$ scattering contribution fixed as part of the core contribution. In the initial stages of refinements, constraints were applied to chemically equivalent atoms. These were released progressively at the end of the refinement. The $\kappa$ coefficients of H atoms were restrained to the value 1.160(1).[37] The $\kappa'$ coefficients of the H atoms bound to C were restrained to the values reported previously,[38] namely, 1.18 with an allowed standard deviation of 0.001. The total number of electrons was kept constant to ensure electroneutrality of the complexes. The C—H bond lengths were restrained to their average neutron diffraction distances.[39] The anisotropic displacement parameters for the H atoms were estimated by using the *SHADE*2 web server[40] and fixed throughout the refinement.

The refinement resulted in featureless residual density maps (**Figure S1**) and converged with a final agreement factor of w$R$(F) = 2.10% and 1.70 % for [**1c**]($CF_3SO_3$) and **1z** respectively (**Table 1**), reflecting the better crystal quality for the **1z** complex. These low values demonstrate the high quality of the synchrotron data and refinement model. The Hirshfeld rigid-bond test[41] carried out after the multipole refinement was satisfactory. For all C—C bonds the greatest difference between mean squared displacements amplitudes never exceeds ($\Delta Z^2 = 5(1) \times 10^{-4}$ Å$^2$), indicating an excellent deconvolution of thermal motion and electron density. As expected, the Rh1—C had significantly higher mean-squares displacement amplitudes along the bond directions ($\Delta Z^2 = 18(2)$–$30(3) \times 10^{-4}$ Å$^2$) exceeding the limit proposed by Hirshfeld ($1 \times 10^{-3}$ Å$^2$) for organic molecules. This is a consequence of the significant difference in atomic masses between Rh and C atoms and of the nature of the metal-to-ligand bonding (Rh1—C=C). A successful rigid bond test may be expected only for a metallocyclic system as previously alluded by Macchi *et al.*[42]

The topological analysis of the experimental electron density and the bond critical points (BCP) localization and properties was performed using the *VMoPro*[34] and *MoProviewer* [34] Programs The experimental atomic properties (atomic volumes and charges) were obtained by numerical integration over the atomic basins using the program *WinxPRO* 2009.[43]

# 3. COMPUTATIONAL METHOD

## 3.1 Datasets and Labeling Conventions

Six sets of data are analyzed and compared in this paper, three for each of **1c** and **1z**. Two sets of data are generated from the X-ray crystallographic experiment. The experimental sets of data for **1c** and **1z** are referred to as **C**-Xry and **Z**-Xry, respectively.

Four sets of data are obtained from quantum chemical calculations, two for each of **1c** and **1z**. One set is obtained from a single point calculation at the crystalline geometry, and the second set is obtained after a full (unconstrained) geometry optimization in the vacuum-phase starting from the crystalline geometry. The first set will be labeled "sp" (*i.e.*, single point), the second set as "opt" (*i.e.*, fully optimized). These calculations in reference to **1c** (**1z**) are labeled **C**-sp (**Z**-sp) and **C**-Opt **(Z**-Opt), respectively.

## 3.2 General Approach and Electronic Structure Methods

All electronic structure calculations were performed on single isolated molecules (*i.e.*, *in vacuo*) without the counterion (present in the crystal of [**1c**]($CF_3SO_3$)) or solvents. To balance accuracy and the cost of the calculations, the chosen electronic structure method is the density functional theory (DFT)[44,45] hybrid functional B3LYP[46,47] along with a *locally-dense basis set* (LDBS)[48-51] being the most dense at the Rh atom and its immediate surroundings, followed by a smaller (but still large) basis set for the intermediate surroundings, and finally by the smallest atomic basis set centered on atoms that are remote from the Rh1 atom (*vide infra*, Section 3.3).

The calculation of an electron density that is both *accurate and continuous* in the region surrounding the Rh atom represents a challenge. First, the size of this system is relatively large (66/65 atoms for **1c** and **1z**, respectively, and 254 electrons counting all the electrons of Rh). Given this size, a basis set is chosen to best represent the region surrounding the Rh atom while minimizing the computational effort spent on the less-relevant organic moities that are distal to Rh in **1c** and **1z** (*vide infra*). A practical approximation to account, implicitly, for relativistic effects is the representation of the core electrons of the metal by an effective core potential (ECP) (also termed pseudopotential, PP).[52-54] While a formally non-relativistic Hamiltonian is employed, the ECP employed in this work, aug-cc-pVDZ-PP,[54] captures relativistic effects empirically, in addition to being correlation consistent.[54,55] The second difficulty is associated with the topological analysis of electron densities obtained from calculations omitting core electrons due to the use of the ECP.[56] Such densities lack nuclear maxima at the nuclear positions of heavy atoms treated by the ECP approximation. Consequently, the densities so obtained exhibit pathological topologies around the boundary(ies) of the core(s) replaced by the ECP.

These problems have been solved in an approximate manner by the recent pioneering work of Keith and Frisch.[57] Their approach essentially restores back the missing electron density after the electronic structure calculation converges and the density ($\rho_{\mathrm{ECP}}$), missing the core, is generated. This is achieved by augmenting $\rho_{\mathrm{ECP}}$ by the missing corresponding closed-shells obtained from an all-electron scalar-relativistic density of the ground state isolated atom.[57] Keith and Frish calculated the atomic densities of all the elements of the periodic table using the

DFT/B3LYP hybrid functional[46,47] with the (large) universal Gaussian basis set (UGBS)[58] and with the incorporation of scalar-relativistic effects through the use of a Douglas-Kroll-Hess second-order Hamiltonian (DKH2).[59-62] The algorithm for augmenting the calculated $\rho_{\mathrm{ECP}}$ with the missing cores has been implemented in the latest version of the Gaussian program[63] which was used in all electronic structure calculations and geometry optimizations.

Upon geometry optimization convergence, the residual maximum force and residual root-mean square forces on the nuclei of **1c** were $2.8\times10^{-5}$ and $5\times10^{-6}$ and those of **1z** were $3.1\times10^{-5}$ and $5\times10^{-6}$ hartree/bohr (atomic units (au)), respectively. The analysis in accordance with the QTAIM[15-17] was performed on the densities generated at the same level of theory of the optimization and of the single point calculations by the use of AIMAll/AIMStudio suite of programs.[64]

In total, 262 atomic integrations were performed. The average magnitude of the 262 atomic Lagrangians is 0.00014±0.00018 au, with no single value exceeding 0.00109 au in magnitude.

## 3.3 Basis Set for Atoms other than Rhodium

As mentioned above (Section 3.2), the electronic structure calculations were performed using a basis set that is densest at and in the immediate vicinity of the Rh atom. This locally dense basis set approach has been shown to provide an excellent balance between accuracy and practical feasibility of the calculation.[48-51]

Correlation-consistent polarized atom-centered triple-ζ quality basis functions augmented with diffuse functions (aug-cc-pVTZ) are placed on all atoms (except P) that are formally bonded and/or in the immediate vicinity of the Rh atom ($d_{\mathrm{Rh}-FAL} \leq 2.3$Å). These atoms (N1, C12, C13, C16, and C17), along with the P atom, will be referred to as the "*first atomic layer* (FAL)". For the phosphorus atom, the basis aug-cc-pV(T+*d*)Z that includes tight *d* functions[65] has been used and was obtained from EMSL basis set exchange website.[66] The inclusion of tight *d* functions on second row atoms is highly recommended for accurate work and is known to alter bond lengths and energetics significantly even at the Hartree-Fock level of theory.[65,67] Next, atoms that are directly bonded to any of the atoms of FAL will be labeled "SAL" (*i.e.*, *second atomic layer*). The SAL atoms (C2, C3, C8, C9, C10, C11, C14, C15, C18, and C19) are described by a correlation-consistent polarized atom-centered double-$\zeta$ quality basis functions augmented with diffuse functions (aug-cc-pVDZ). Finally, all remaining atoms are described by the same basis set but without the diffuse functions, *i.e.* by the cc-pVDZ atom-centered basis set.

## 3.4 Basis Set and Effective Core Potential for the Rhodium Atom

The aug-cc-pVDZ-PP[54] ECP was used to replace 28 core electrons ([Ar]3$d^{10}$) of Rh. This core size has been recommended by Peterson *et al.* as it has been shown to achieve a good spatial and energetic separability of core and the explicitly treated 17 valence electrons of Rh (electrons: $4s^2,4p^6,4d^8,5s^1$). This ECP has been optimized for Y-Pd 4*d* transition elements and has been shown to reproduce atomic valence spectra obtained from four-component all-electron multi-configuration Dirac-Hartree-Fock calculations.[54]

# 4. RESULTS AND DISCUSSION

**Figure 1** shows the crystal structure of the two studied complexes, the cationic complex $[(C_{25}H_{38}NPRh)]^+(CF_3SO_3)^-$ ([**1c**]($CF_3SO_3$)) and the zwitterionic analogue ($C_{25}H_{37}NPRh$) (**1z**), along with the numbering scheme. Selected bond lengths and angles for both complexes are listed in **Table S.1** while **Tables S.2** and **S.3** list their experimental and optimized Cartesian coordinates (see the Supporting Information).

## 4. 1 Crystal Packing

A view of crystal packing of the two complexes is displayed in **Figure 2**. The crystal structures of the two compounds are similar and both form monoclinic crystals as described in **Table 1**.

***Salt of the Cationic Complex [1c]($CF_3SO_3$).*** The crystal packing of [**1c**]($CF_3SO_3$) is built from chains of $(C_{25}H_{38}NPRh)^+$ cations running along the crystallographic ***a*** axis and alternating with the $(CF_3SO_3)^-$ anions (**Figure 2**). The cationic chains and the anionic moieties are connected via anion-cation electrostatic forces and through eight C—H···O intermolecular interactions and two C—H···F weak contacts (C9—H9···F1 and C18—H181···F2) (**Table 2**). Each $(C_{25}H_{38}NPRh)^+$ cation interacts with five $(CF_3SO_3)^-$ neighbouring anions. All oxygen atoms of the $(CF_3SO_3)^-$ anionic group are involved in hydrogen bonds: O2 acts as an acceptor four times, O1 three times, while O3 is acceptor only once. There are no π-π interactions between the aromatic rings in the crystal packing. The molecular structure can be viewed as a donor-acceptor adduct, in which the $(CF_3SO_3)^-$ group plays an important role in the observed intermolecular interaction pattern.

***Zwitterionic Complex 1z.*** The molecular crystal packing of **1z** is composed of zigzag chains along the ***c*** axis (**Figure 2**) by the means of two categories of intermolecular interactions: two C—H···C interactions and three C—H···π system contacts (**Table 2**). Each molecule is surrounded by four symmetry-related molecules. The zigzag chains along the crystallographic ***c***

axis are linked through the weak C18—H182···C3A interaction between the cyclooctadiene group and the aromatic rings. These zigzag chains are interconnected through another weak hydrogen bond C7—H7···C23 (**Figure 2**)**.** As clearly depicted in **Figure 2**, the nearly perpendicular orientation of the cyclic group explains the absence of π···π interactions between the aromatic rings in the crystal packing.

## 4. 2 Molecular Geometries in the Vicinity of the Rhodium Atom

The rhodium atom is tetra-coordinated in both complexes, considering each olefin as a single ligand. On the basis of the bond path connectivity, however, the Rh atom can be considered as hexa-coordinated since it is normally linked to an olefin ligand by *two*, rather than one, bond path. The metal atom is bonded to the two alkene groups of the COD ligand (C*n*, *n* = 12, 13, 16, 17), as well as to phosphorus P1 and nitrogen N1 of a P,N-bidentate ligand. (See **Figure 1**).

The four alkene carbon atoms of the COD ligand are not symmetrically linked to the Rh atom. Indeed, one can observe that, firstly, in both complexes the Rh1—C13 bond distance is approximately 0.04/0.05 Å (Xry/Opt) shorter than the Rh1—C12 even though both are *trans* to the P1 atom. On the other hand, in **1c** the Rh1—C16 bond is significantly longer compared to the Rh1—C17 bond (by 0.04/0.04 Å (Xry/Opt)); however, it is only slightly longer by only 0.01/0.01 Å (Xry/Opt) in **1z**. These differences in the Rh–C bond lengths are consistently reproduced in the optimized and experimental geometries and therefore can be reasonably attributed to the internal electronic structure of the molecules rather than crystal packing effects. Secondly, the Rh—C (COD) bond lengths *trans* to the phosphorus atom P1 are significantly longer than those *trans* to the nitrogen atom N1 in both **1c** and **1z**. These observations are in keeping with the greater *trans* influence of phosphorus over nitrogen, and are similar to what has been found in other related Rh complexes.[68]

The detailed examination of the square-planar arrangement around the rhodium atom reveals two significant imperfections: First, the Rh1 atom is closer to the centers of the double bonds (C12=C13 and C16=C17) than to the nitrogen (N1) and phosphorus (P1) atoms, and the P1–Rh1–N1 bond angle deviates from 90°: Its value in **1c** is 86.5/83.4º (Xry/Opt), and in **1z** it is 85.8/83.2º (Xry/Opt) and in both cases is likely attributable to the geometric requirements of the bidentate P,N ligand. The deviations from 90º are thus quite similar in the two compounds and reasonably well-reproduced computationally.

As alluded to above, the distance between the mid-point (centroid) of the coordinated C12=C13 bonds (*trans* to P1) and the Rh1 atom is ~ 0.1 Å longer than those between the Rh1 atom and the C16=C17 bonds (*trans* to N1), in keeping with the greater *trans* influence of phosphorus over nitrogen. Specifically, the Rh-alkene distance is longer by 0.09/0.11 Å (Xry/Opt) in **1c**, and 0.13/0.12 Å **1z** (Xry/Opt). Further, the nitrogen (N1) atom, the phosphorus (P1) atom, the rhodium (Rh1) atom and the centroids of the double-bonds are not strictly coplanar. Whereas the double bond centers do not deviate significantly (0.00/0.05 and 0.12/0.07 Å, Xry/Opt) from the mean plane defined by the rhodium, phosphorus and nitrogen atoms in **1z**, their deviations are more important in **1c** (0.56/0.50 and 0.37/0.40 Å (Xry/Opt)). Again, the close agreement between experimental and optimized deviations from the plane suggests that these geometrical differences are characteristics of the molecules themselves rather than being a result of crystal packing.

An important point to note in the above geometrical comparisons is that the agreement between the optimized and the experimental geometry is slightly, but consistently, better for the zwitterionic compound (**1z**) than it is for the cationic compound (**1c**). This is probably due to the fact that while there are no counterions in the crystal of **1z**, the presence of the polar counterion in the crystal of **1c** is not addressed in the vacuum-phase optimization of the cationic portion of **1c** (carried out without the counterion).

Striking differences in the interatomic distances within the five-membered ring (5-MR) of the indene-derived fragment distinguish the cationic complex **1c** from its zwitterionic analogue **1z**. Thus, in the cationic form the (5-MR) ring exhibits bond length alternation that characterizes non-aromatic rings; bonds C1—C7A (1.5109(5) Å), C1—C2 (1.5116(5) Å) and C3—C3A (1.4886(4) Å) are formally single bonds, whereas C2—C3 (1.3643(3) (Å) and C3A—C7A (1.4161(5) Å) are formally double bonds. In the zwitterionic form **1z**, the indenide unit possesses a highly delocalized ring structure with the accompanying equalization of bond lengths in the 5-MR, consistent with a Hückel aromatic (4*n*+2) 10π–electron indenide anion (see **Table S.1** of the Supporting Information for selected geometrical parameters).

## 4. 3 Molecular Graphs

A molecular graph consists of the network of bond paths[69-71] defining the chemical structure in real three-dimensional space.[15-17] A bond path is found to link the nuclei of atoms considered bonded on the basis of chemical and spectroscopic evidence, with no counter example(s) known to us. In other words, the molecular graph recovers the chemical structure. The presence or absence of a bond path is an all-or-none feature that does not distinguish, by itself, between the bonds of different order, strengths, or modes.

Weak and border-line interactions are generally more ambiguously assigned on the basis of empirical evidence. In these cases, the bond path is a definitive indicator of chemical bonding when it exists, however, the absence of a bond path does not always negate an imminent bonding interaction. This is so because, in contrast to strong interactions, the presence or absence of a bond path of a weak bond can be highly sensitive to small electronic and/or geometrical changes. In these cases, an invaluable indicator of bonding is the delocalization index (DI or $\delta(A,B)$),[72] also defined within QTAIM. This index is a continuously varying indicator of bonding that has been shown to be elevated between atoms sharing a bond path.[73,74] The DI constitutes a measure of the bond order that is exponentially correlated with the density at the bond critical point when a bond path exists.[75] An extensive description of the usage of DI in organometallic chemistry is given by Macchi and Sironi.[76]

The molecular graphs for the two complexes obtained from the theoretical densities after full energy minimization in the vacuum phase are displayed in **Figure 3**. (The molecular graphs obtained from the experimental densities and those calculated at the experimental geometries can also be found in Fig. S2). The bond paths of strong interactions (arbitrarily defined as exhibiting values of $\rho_b \geq 0.05$ au) are displayed as solid gray lines linking the nuclei of the interacting atoms. Bond paths of weak interactions ($\rho_b < 0.05$ au) are plotted as pink solid lines in the experimental graphs, and as dotted lines in the calculated graphs. The weak interactions found in these complexes are exclusively of the *hydrogen–hydrogen* (or H–H) bonding type where two closed-shell neutral (or similarly charged) hydrogen atoms share a bond path $\mathrm{H}^{\delta\pm}\cdots\mathrm{H}^{\delta\pm}$.[77-80] (The H–H bonding is distinct from the *dihydrogen* bonding $\mathrm{H}^{\delta\mp}\cdots\mathrm{H}^{\delta\pm}$, a hydrogen bond whereby the proton acceptor is a hydridic hydrogen atom).[81] While the pattern of H–H bonding in these complexes is very interesting and contributes to their overall structural stability, a detailed discussion of such phenomena is beyond the scope of this manuscript and will be described in detail elsewhere.

The sub-molecular graphs that include only strong bonding interactions of the two complexes are similar, whether obtained from the X-ray density or calculated at the experimental or optimized geometries. The similarity is not only across the three molecular graphs of **1c** or **1z** but also between these two complexes (with the exception of the additional covalent C1–H2 bond present in the 5-MR of **1c**). A difference between the calculated and experimental molecular graphs is that, in all four theoretical densities, the bond path linking the nuclei of Rh1 and C13 is not observed, as is also the case in the experimental graph of **1z**. It is also noteworthy that the high ellipticity of the Rh1—C13 bond, which reflects the flatness of the density in this region, is such that a small perturbation in the charge density can lead to its disappearance and a "catastrophic" change of structure.[15] Similarly unstable bond paths have already been observed in numerous transition metal complexes.[82,83]

## 4. 4 Bond Properties at Rhodium

The properties of the bonds surrounding Rh are collected in **Table 3**. In the following discussion, and when quoting numerical values from **Table 3**, data will be quoted in the order (Xry/sp/opt). All three sets of numerical entries are generally different with the exception of bond lengths, since their values from the Xry and sp sets are identical. Finally, there are no entries for the delocalization index in the Xry data set since this quantity is only available from theoretical calculations, as it necessitates the atomic overlap matrix of spin orbitals.

The three datasets entered in **Table 3** exhibit a remarkable quantitative agreement (especially between Xry and sp values), not only among themselves for a given complex, but also and importantly, between the two different complexes. The similarity of the bonding descriptors of **1c** and **1z** is consistent with a largely unaltered catalytic Rh center in the zwitterion **1z** which is, therefore, anticipated to have a similar activity to the parent compound, namely, the cationic complex **1c**. All listed bond properties, including those known to be particularly sensitive such as the Laplacian at the bond critical point (BCP), generally exhibit this relatively close similarity. Further, a given bond exhibits similar properties in both compounds, whether by comparing the experimental or both sets of calculated properties.

***Bonds involving the Rh atom, generalities.*** The experimental static deformation density map around the Rh metal center for **1z** is shown in **Figure 4(a)** (plane Rh1-P1-N1). A similar plot is found for the corresponding plane in **1c** (not shown). The typical 4*d* electron density for Rh1 atom is clearly revealed by the aspherical density accumulation near the Rh1 atom directed towards the metal-ligand bisectors and by the charge depletion pointing towards the ligand. **Figure 4(b)** illustrates the map of the negative Laplacian function of the experimental density through the same plane (Rh1-P1-N1). As expected from ligand field theory, the pronounced regions in which the valence density is locally depleted are observed along the Rh1-ligand directions, whereas the valence electron concentrations bisect the ligand directions.

We remark first that all six bonds involving the Rh atom are characterized by a relatively low electron density at the BCP ($\rho_b$), reaching a maximum of only ~ 0.10-0.11 au in the case of bonding to the phosphorus and the carbon atoms (**Table 3**). In all cases, bonds with the Rh1 are all characterized with a positive Laplacian ($\nabla^2\rho_b$). This is a reflection of the minimal accumulation of density near the interatomic surfaces involving that atom, as can be gleaned from the small magnitudes of the negative curvatures ($\lambda_1$ and $\lambda_2$) compared to the magnitude of the positive curvature ($\lambda_3$).

The low magnitude of $\rho_b$ and the positive $\nabla^2\rho_b$ are both characteristics of closed-shell interactions. On the other hand, all bonds involving Rh1 also exhibit a significant degree of electron sharing or "covalency". The electron sharing (or delocalization) index (DI or $\delta(A,B)$),[72] which provides a counting of the number of electron pairs shared between two given atomic basins *A* and *B*, shows that all the bonds involving the Rh1 atom have a significant level of sharing with $\delta$(Rh1,*X*) falling in the range of 0.51–0.89 pairs. This degree of electron sharing is far greater than that of a closed-shell interaction, whereby the DI can fall to less than ~ 0.1 pairs, since there is no significant exchange between the two closed-shell atoms.

An independent measure of the covalency of a bond is the sign and magnitude of the total energy density at the BCP ($H_b = G_b + V_b$).[84] In covalent bonds, $H_b$ is typically negative and of a non-negligible magnitude. **Table 3** shows that $H_b$ values are negative for all interactions involving Rh1, but that their magnitudes are generally small, reaching a maximum magnitude of only 0.05 au in the case of Rh1–P1 only. This criterion indicates some covalency, but that it is not pronounced, thereby confirming the conclusions drawn on the basis of $\rho_b$, $\nabla^2\rho_b$, and $\delta$(Rh1,X).

Moreover, and according to the classification of Macchi *et al.*,[42] the nature of the Rh1—C*n* bonds clearly differs from that of purely ionic bonds (closed-shell): Firstly, the Rh1—C=C bond path topologies clearly show two independent endocyclic curved bond paths (**Figure 5**). This is in clear contrast to the purely closed-shell interactions that would have resulted in a T-shaped structure, as previously reported by Scherer and co-workers in their experimental electron density analysis of scandium carbide complexes.[85] These inward curvatures are consistent with the classical Dewar-Chatt-Duncanson (DCD) model[86,87] as discussed earlier by Macchi *et al.*[42,88,89] and in other recent electron density studies.[90] There has been some recent interest in this type of bent bond paths occurring, for example, in the case of bonding between Co and a C=C double-bond.[91]

On the other hand, the bond paths for Rh1—C*n* interactions are longer than the interatomic distances (see **Table 3**), reflecting that these interactions are not those of an ideal metallacycle characterized by a straight M—C bond paths. Thus, not all the bonds involving the

Rh1 can be simply classified into one category, since they have some of the characteristics of both closed-shell and covalent bonding. We now discuss each bonding interaction occurring in the vicinity of the metal center.

***Rh1–N1 bond.*** This bond is slightly longer in **1z** compared to **1c** in the optimized geometries (by 0.002 Å) and have the same tendency in the experimental data with a difference of 0.013 Å. The optimized bond length is longer than the experimental one by 0.047 Å and 0.036 Å for **1c** and **1z**, respectively. The electron density at the bond critical point, $\rho_b$, in the case of **1c** is (0.078/0.075/0.068) and is (0.075/0.075/0.069) for the **1z** complex, indicating a very similar bond order/strength. The electron density at the Rh1-N1 BCP is relatively low ($\rho_b \approx$ 0.07-0.08 au) when compared to a (polar) covalent bond such as N1-C2 ($\rho_b \approx$ 0.25-0.28 au), as may be expected (**Table 3**). The sharing index in both complexes indicates a very similar sharing of ~ 0.5 pairs between Rh1 and N1.

***Rh1–P1 bond.*** Experimentally, this bond is of equal length in both **1c** and **1z** within experimental uncertainties. In the optimized geometries, however, this bond in **1z** is slightly longer than its counterpart in **1c** by 0.034 Å. Further, the optimized bond length is longer than the experimental one by 0.029 Å and 0.062 Å for **1c** and **1z**, respectively. For **1c**, $\rho_b$ has the values (0.095/0.103/0.098) which are close to those in **1z** (0.103/1.06/0.095). These values of the electron density at the Rh1–P1 BCP are slightly higher than any of the other Rh–*X* bonds in the two complexes (**Table 3**). The particularly good agreement between all the Rh1–P1 bond properties obtained from the experiment and the single-point calculation adds further support to the quality of the basis set and the underlying level of theory including the recommended addition of a set of tight *d* functions.[65]

***Rh1–C*****n** ***(*****n** **=** ***12, 13, 16, 17) bonds.*** The bond paths associated with these interactions are all observed in the six datasets, with the exception of the Rh1–C13 bond path which is only observed in the experimental density of the **1c** complex. The elevated ellipticity of the Rh1–C13 bond path is indicative of a topologically unstable interaction (vide supra). In the calculated densities, this bond critical point has coalesced with the ring critical point, annihilating the corresponding (unstable) bond path. It is unsurprising that they are not observed in any of the four calculated densities. Once again, experiment and theory yield a consistent picture.

Comparing the two arms of the Rh1–C12–C13 triangle, the Rh1–C12 distance is shorter in both compounds and in both the calculated and experimental geometries than the Rh1–C13 distance. The differences ($d_{\mathrm{RH1–C12}}$ – $d_{\mathrm{RH1–C13}}$, in Å) are: –0.042 (**C**-Xry/sp), –0.054(**C**-opt), –0.036 (**Z**-Xry/sp), and –0.047(**Z**-opt). In the optimized geometry of **1c**, Rh1–C13 is also longer than Rh1–C12 by 0.0536 Å, with this difference being very similar to that found in the optimized geometries of **1z** (0.0471Å). These geometrical comparisons indicate that the two interactions are very similar in the two complexes. The lack of the Rh1–C13 bond path represents an exemplary case whereby the DI is invaluable in quantifying an incipient bonding interaction.

The strength of the Rh1–C13 interaction, as measured by the DI, shows very little discrepancy for both **1c** and **1z** relative to the DI for Rh1–C12 in both complexes. The values of the DI in both compounds and both bonds, whether from the sp or opt calculations compare very well. Thus, to two decimals, we have: [**1c**]/[**1z**], $\delta$(Rh1,C12) = [0.55/0.52]/[0.52/0.53], and $\delta$(Rh1,C13) = [0.51/0.48]/[0.50/0.50]. The corresponding differences ($\delta$(Rh1,C12) – $\delta$(Rh1,C13)) are: 0.04 (**C**-sp), 0.04 (**C**-opt), 0.02 (**Z**-sp), and 0.03 (**Z**-opt). The magnitudes of these differences indicate an insignificant variation in the extent of electron delocalization between the Rh1 and both carbon atoms, which can be taken as 0.5 pairs. The two bonds, Rh1–C12 and Rh1–C13, can, thus, be expected to be of comparable strength in both complexes.

All descriptors of bonding indicate that the Rh1–C16/Rh1–C17 bonding interactions ($\rho_b$ ranging from 0.091–0.104 au; *trans* to N) are significantly stronger than the Rh1–C12/Rh1–C13 pair ($\rho_b$ ranging from 0.073–0.082 au; *trans* to P) in both complexes. The $\rho_b$ values listed in **Table 3** indicate that the two bonds (Rh1–C16 and Rh1–C17) have very similar values in all datasets, with a modestly stronger Rh1–C17 interaction in both complexes. Even this subtle difference appears to be reproduced quite faithfully in the two complexes **1c** and **1z**. The sharing index ranges from 0.65 to 0.71, and therefore both bonds in the two complexes engender a delocalization of ~ 0.7 pairs between the rhodium and the carbon atoms.

***Remaining bonds around Rh1.*** There is nothing unusual in the topological properties of the remaining bonds: N1–C2, P1–C3, C12–C13, C16–C17, and C2–C3. All of these bonds in both compounds and in all data sets exhibit, without exception: a negative Laplacian at the BCP; a negative total energy density $H_b$ with a magnitude and order higher than the bonds involving the Rh1 atom; high values of $\rho_b$; and an elevated $\delta(A,B)$. The properties of these bonds listed in **Table 3** also indicate that experiment and theory are in good agreement and that the bond properties in the zwitterionic complex **1z** are very similar to their counterparts in the cationic complex **1c**.

## 4.5 The Properties of the Atoms Proximal to Rhodium

**Table 4** provides a listing of some basic QTAIM topological properties for both complexes: Atomic charges $q(\Omega)$, atomic electron populations $N(\Omega)$, atomic volumes Vol($\Omega$), and atomic energies $E(\Omega)$. The values of $q(\Omega)$, $N(\Omega)$, and Vol($\Omega$) are for the three data sets. The listing of

$E(\Omega)$ in the table is exclusively for the "opt" dataset since only in this case are the virial-based atomic energies defined without the necessity of a heuristic partitioning of the term arising from virial of non-vanishing forces on the nuclei. The table lists the individual atomic properties of Rh and its immediate surrounding atoms only, namely, the six atoms sharing a bond path with Rh. The properties of the remaining of the atoms are included in the sum of the group to which they belong (**Table 4** and **Figure 6**). **Figure 6** depicts the summed atomic properties on five chosen groups that represent the different regions surrounding Rh. The groups include P*i*$Pr_2$, COD, $NMe_2$, the indene/indenide moiety, and the Rh center itself.

***Precision of the numerical atomic integrations.*** As can be seen at the bottom of **Table 4**, the sum of all the atomic charges for **1z** is (0.023/0.002/0.003) au for the three datasets. For a system with 254 electrons, this constitutes a numerical integration error of (0.01/0.00/0.00) %, respectively. In the case of **1c**, the sum of atomic charges is 0.999 and 1.000 au for the "sp" and "opt" datasets, with an error of 0.00% in both cases. In the crystal, each molecule of **1c** (254 electrons) is accompanied by counterion molecule ($CF_3SO_3^-$) bearing 74 electrons. The number of electrons in the neutral salt (i.e., [**1c**]($CF_3SO_3$)) is, thus, 328 electrons. The sum of all charges for a neutral pair (**1c** featuring its counterion) is 0.488 au instead which yields a global relative error of 0.15% (0.488/328), higher than in the case of **Z**-Xry but still acceptable and in line with other experimental results. This error is probably due to the more diffuse density in the inter-ions region and larger integration volume of the cation-anion pair compared to the more compact single-component molecular species in the case of the zwitterions **1z**. The quoted experimental atomic electron populations $N(\Omega)$ that are listed in **Table 4**, thus, can be considered as having an uncertainty of ~ 0.2% of their quoted value due to this integration error.

***The Rh1 atom.*** All three datasets for both the cation **1c** and the zwitterion **1z** indicate a net charge on Rh of *ca.* +0.3–0.4 au. The net charge on this atom seems to be very slightly higher in **1z**, in keeping with the conceptual view that the design of the zwitterionic complex **1z** succeeds in emulating the characteristics of the cationic species **1c** with respect to the net charge at Rh. In all cases $q_{\mathrm{opt}}(\mathrm{Rh1}) > q_{\mathrm{sp}}(\mathrm{Rh1}) > q_{\mathrm{Xry}}(\mathrm{Rh1})$, where the magnitude of the difference $|q_{\mathrm{opt}}(\mathrm{Rh1}) - q_{\mathrm{Xry}}(\mathrm{Rh1})|$ equals to 0.063 au in **1c** and 0.074 au in **1z**. These results are consistent with the lower level calculations carried out on truncated models (Level 2, **1c′** and **1z′**; **Chart 1**), whereby the charge on the Rh1 was found to be +0.33au in **1c′** and +0.36 au in **1z′**; for comparison, at the higher level (Level 1), $q(\mathrm{Rh1}) \approx +0.35$ au **1c** and $\approx +0.37$ au in **1z**.

The volume of the Rh1 atom is consistently slightly larger in **1z** than in **1c** (by 0.2/4.6/4.2 au) despite the atom's slightly lower electron population in the former complex. The lower energy of the Rh1 in **1c** indicates a higher stability (by 24 kcal/mol) of the outer-shell electrons (treated explicitly) compared to **1z**. A more stable Rh1 in **1c** is consistent with its slightly higher electron population than in **1z**. However, these observations regarding the stability of the Rh1 atom do not take into account core polarization, which is nonexistence in the present calculations. Furthermore, there is no evidence in experimental maps of any core polarizations (see **Figure 2**). Again, at least within the selected atomic properties, the characteristics of the Rh1 atom appears to be very similar in the nearly isostructural complexes **1c** and **1z**, and as such would be expected to have a similar chemistry, perturbed to some extent by the differing electronic environments in the two related complexes.

***The P1 atom.*** This atom is consistently more positively charged in the theoretical model (by 0.138/0.116 au) in the zwitterionic complex **1z** than it is in the cationic relative **1c**. Of particular interest with regard to the conventional organometallic representations that are employed for such complexes is the observation that in both cationic **1c** and neutral **1z** the P atom, not the Rh atom, bears the greater net positive charge. This P atom is more compact in **1z** (its volume being smaller by 4.8/4.8/2.7 au) and considerably less stable than in **1c** (by 57.8 kcal/mol).

***The N1 atom.*** This atom is more negatively charged in the calculated densities (by 0.155/0.023 au) in the zwitterionic complex **1z** than it is in the cationic complex **1c**, in keeping with the electronegative nature of N, and pointing to "leakage" of electron density from the indenide unit in **1z**. This atom, however, bears an equally negative charge in the two complexes within experimental uncertainties. This atom is smaller in size in **1z** (by 1.0/0.5/0.4 au) but almost isoergic with respect to its counterpart in **1c** (less stable by 1.9 kcal/mol).

***The C*n *(***n = ***12, 13, 16, 17) atoms.*** The carbon atoms bonded to Rh1 are all negatively charged (with $q(\mathrm{C}n) \approx -0.1$ to $-0.4$ au) without exhibiting striking trends in atomic properties.

## 4.6 Comparison of Group Properties in 1c and 1z

**Figure 6** displays the net charge ($q$) and the volume (Vol.) of five regions in **1c** (in atomic units) obtained from the "opt" set of calculation. The changes in these properties, $\Delta q$ and $\Delta$Vol., respectively, as well as the changes in the energies $\Delta E$ (in kcal/mol) for these five groups are given for **1z**.

The group properties and their changes upon the formal removal of the C1–H2 proton from **1c** to give **1z** are revealing (**Figure 6**). First, the total complex energy rises considerably by the removal of this proton, with the overall change in the energy of the reaction (i.e., **1c** → **1z** + $\mathrm{H}^+$ = 273 kcal/mol) being primarily due to the loss of more electron-nuclear attractive (negative) energy than the reduction in the nuclear-nuclear repulsion. The loss of the H2 proton also causes the total electron density of the system to be slightly more diffuse, thus the volume increases by ~

28 atomic units in **1z** compared to **1c** (despite of having one less atomic basin in **1z**). In percentage terms, however, the change in the volume due to the removal of the proton is only *ca.* –0.8%. This energetic destabilization also overwhelms the necessarily stabilizing increase in the magnitude of the quantum exchange between the basins of the indenide fragment with its extended aromaticity in **1z** (two fused aromatic rings), relative to an isolated aromatic (benzene) ring in **1c**. Along with the bond lengths equalization, the indenide ring system becomes considerably more aromatic in **1z** compared to the indene unit in **1c** (the nucleus independent chemical shift (NICS)[92,93] calculated at the centroids of the 6-MR and 5MR for the two compounds are: –13.7 and –1.8 ppm for **1c**, and –14.8 and -21.7 ppm for **1z**, respectively (**Table S.4**)).

The destabilization of **1z** with respect to **1c** is associated primarily with the indenide framework (+285 kcal/mol), but also from the Rh1 atom itself (+24 kcal/mol), when compared to their counterparts in **1c**. In **1z** (compared to **1c**), electronic charge is transferred from Rh1 to all of its neighbouring groups. Thus, the $R_P$ group gains 0.06 electrons, increases in volume by 3.3 au, but is destabilized by 16 kcal/mol; the $R_N$ group gains 0.08 electrons, increases in volume by 1.9 au, and is stabilized by 22 kcal/mol; and the COD group gains 0.14 electrons, increases in volume by 6.0 au, and is stabilized by 30 kcal/mol. Together, the three groups attached to Rh1 acquire 0.28 electrons, expand in size by 11.2 au, and are stabilized, as a result, by a total of approximately 36 kcal/mol. When the changes of the all groups except those associated with the indene (**1c**)/indenide (**1z**) fragment are summed together, this subsystem gains a total of 0.27 electrons, increases in size by 19.6 au, and is stabilized by only 12.4 kcal/mol; when summed with $\Delta E$(indenide–indene) the energy difference between the two complexes is obtained.

These observations indicate that the response of complex **1c** to the loss of proton H2 (thereby transforming the indene structure in **1c** into an indenide fragment in **1z**) results in a drastic electronic structure reorganization, primarily within the incipient indenide framework, leaving the essential features of the Rh1 and its immediate surroundings relatively unchanged in **1z** relative to **1c**.

## 4.7 Topography of the Molecular Electrostatic Potential (ESP) ($V(\mathbf{r})$)

The molecular electrostatic potential (ESP), $V(\mathbf{r})$, is defined:

$$V(\mathbf{r}) = \sum_A \frac{Z_A}{|\mathbf{R}_A - \mathbf{r}|} - \int \frac{\rho(\mathbf{r}')}{|\mathbf{r}' - \mathbf{r}|} d\mathbf{r}' \qquad (3)$$

where $Z_A$ is the charge of nucleus $A$ at the position $\mathbf{R}_A$, and $\rho(\mathbf{r}')$ is the electron density obtained from theoretical calculations or from multipolar modelling.[94]

The evidence presented in the previous sections suggests that the primary region of interest with regard to stoichiometric and catalytic reactivity involving **1c** and **1z**, namely, the Rh1 atom and its immediate surroundings, remains unaffected by the formal removal of the proton H2 in **1c** to afford **1z**. The most drastic changes in the bond, atomic, and group properties that accompany this deprotonation are relegated to the carbocyclic backbone of the ancillary P,N-ligand. As can be seen from **Equation 3** the ESP is determined by the *total* charge density that results from two contributions: (a) The discrete distribution of the point-like nuclear charge (first term) and (b) the continuous diffuse electronic charge (second term). The first term is completely determined by the geometry $\{\mathbf{R}_A\}$ (and the nature of nuclei) while the second is determined by the density $\rho(\mathbf{r})$. The similarity of both the geometry and the electron density in the Rh coordination sphere surrounding Rh1 in **1c** and **1z** is tantamount to a similarity of the corresponding region in their respective molecular electrostatic potential. On the other hand, the indene and indenide backbones of the ancillary P,N-ligands in **1c** and **1z** (respectively) are expected to exhibit marked differences given that their geometries, electronic charges, and nuclear potentials are drastically different in the two complexes.

The anticipated similarity of the shape of the ESP in the two complexes, irrespective of the orientation can be visually appreciated from **Figure 7** which gives two side views of the calculated ("sp") ESP for the two opposite "faces" of each of **1c** and **1z**. Furthermore, **Figure 8** compares the experimentally determined ESP of the two complexes; in this case, the ESP of the **1c** complex is determined in the presence of its counteranion. Despite this significant perturbation, the displayed (representative) isosurfaces of the ESP around the Rh centers in **1c** and **1z** do no differ significantly.

Thus the general topography of the ESP of **1z** around the Rh1 atom bears a striking similarity to that around the Rh1 atom of **1c**. Indeed, the differences that arise can be attributed entirely to the differing carbocyclic backbone frameworks in **1c** and **1z.** The ESP in the **1z** complex exhibits a clear demarcation nodal surface (a surface whereby the ESP = 0) that splits the molecule into two parts: A quasi-intact Rh fragment and an indenide moiety that carries the burden of most of the changes (*i.e.*, added negative charge) induced by the formal removal of a proton from C2 in **1c**. **Figures 9** and **10** show a clear demarcation between the two regions of **1z** as can be seen from the shape of the nodal surface in $V(\mathbf{r})$.

Since it is the electric field $\mathbf{E}(\mathbf{r})$ that determines the trajectory of an approaching charged reactant, and since $\mathbf{E}(\mathbf{r})$ is uniquely determined by the ESP ($\mathbf{E}(\mathbf{r}) = -\nabla V(\mathbf{r})$), the shape of the potential determines the direction of approach and then demonstrates the similarity of the metal centered reactivity of both complexes.

## 5. CONCLUD ING REMARKS

Highly accurate electron density distributions of structurally analogous cationic (**1c**) and zwitterionic (**1z**) organometallic complexes were determined from accurate synchrotron X-ray diffraction experiments and a high level of computational theory. The strong agreement found between experimental and theoretical results provides considerable support to the conclusions summarized herein.

A comparison of the geometries, electron distributions, electron delocalization, and molecular electrostatic potentials in these two complexes reveals a striking feature: The two complexes are very similar within the Rh1 coordination sphere, and differ (quite significantly) only with regard to the properties associated with the indene (**1c**) and indenide (**1z**) frameworks. These similarities *and* differences are equally important with regard to confirming the postulate that appropriately designed zwitterionic platinum-group metal complexes (such as **1z**) can serve as charge-neutral variants of more conventional cationic species (such as **1c**) in reactivity applications. Indeed, in keeping with the results of our catalytic experiments,[18] **1z** is predicted to exhibit metal-centered reactivity behaviour that is reminiscent of **1c** due to the minimal steric and electronic perturbation that is observed in the metal coordination sphere on going from **1c** to **1z**. Furthermore, the reasonably efficient sequestration of charge on the conjugated carbocyclic P,N-ligand backbone in **1z** enforces *considerable zwitterionic character* in this species (the indenide fragment carries a charge (in au) of –0.754 (experiment), –0.924 and –0.918 (theory: single point at the experimental geometry and after geometry optimization, respectively) and the rest of the molecule carries an equal and opposite distributed positive charge). We envision that having confirmed herein that donor-substituted indenide ligands can support genuinely zwitterionic (charge-separated) platinum-group metal organometallic complexes that exhibit properties reminiscent of their cationic counterparts will encourage the further development and study of this and other classes of zwitterionic platinum-group metal complexes.

**SUPPORTING INFORMATION:** Includes: **(1)** X-ray crystallographic "cif" files of the two complexes **1c** and **1z**. **(2)** Four Gaussian09 extended wavefunction files of the two complexes, calculated at the experimental and optimized geometries, augmented with Rh core densities. These text-files can also be read by AIMAll/AIMStudio. (3) A pdf file containing: A tabulation of selected experimental and optimized bond lengths and angles (**Table S.1**), tables of experimental and optimized cartesian coordinates (Tables **S.2** and **S.3**, for **1c** and **1z**, respectively), a table listing the correspondence of the experiment atomic numbering/labeling schemes to the serial atomic numbering as in the theoretical wavefunction files calculated from Gaussian09 (**Table S.4**), a listing of the calculated nucleus independent chemical shifts (NICS) at the three ring centers of **1c** and **1z** (**Table S.4**), and finally, comparative plots of the Laplacian of the electron density in three planes containing the rhodium metal from the three data sets for the two complexes (**Figure S3**).

## 6. ACKNOWLEDGEMENTS

The authors are very grateful to Dr. Kevin Hesp (Stradiotto Group, Dalhousie University) for growing the single crystals that were used in this study. E.-E. B. is grateful to Professors Sylvain Ravy and Erik Elkaïm of CRISTAL beamline at SOLEIL Synchrotron for many helpful discussions, and to Drs. Benoit Guillot and Bertrand Fournier for *VMoPro* and *MoProViewer* tutorials. Professor Kirk A. Peterson (Washington State University) is thankfully acknowledged for his useful insight about the use of tight functions on phosphorous atoms. We are also very grateful to Mr. Fabien Legrand (SOLEIL) for technical assistance. C.F.M. acknowledges the financial support of the Natural Sciences and Engineering Research Council of Canada

(NSERC), Canada Foundation for Innovation (CFI), and Mount Saint Vincent University. C. F. M. is also grateful for several Visiting Professorships at the Université Henri Poincaré (now Université de Lorraine) from 2007-2011 during which most of this work has been completed. M. S. thanks NSERC, the Killam Trusts, and Dalhousie University for their generous support of this work.

## References

(1) Knowles, W. S. *Angew. Chem. Int. Ed.* **2002**, *41*, 1999.

(2) Bell, S.; Wüstenberg, B.; Kaiser, S.; Menges, F.; Netscher, T.; Pfaltz, A. *Science* **2006**, *311*, 642.

(3) Schrock, R. R.; Osborn, J. A. *J. Am. Chem. Soc.* **1976**, *98*, 2134.

(4) Schrock, R. R.; Osborn, J. A. *J. Am. Chem. Soc.* **1976**, *98*, 2143.

(5) Crabtree, R. *Acc. Chem. Res.* **1979**, *12*, 331.

(6) Källström, K.; Munslow, I.; Andersson, P. G. *Chem. Eur. J.* **2006**, *12*, 3194.

(7) Macchioni, A. *Chem. Rev.* **2005**, *105*, 2039.

(8) Smidt, S. P.; Zimmermann, N.; Studer, M.; Pfaltz, A. *Chem. Eur. J.* **2004**, *10*, 4685.

(9) Stradiotto, M.; Hesp, K. D.; Lundgren, R. J. *Angew. Chem. Int. Ed.* **2010**, *49*, 494.

(10) Amer, I. ; Alper, H. *J. Am. Chem. Soc.* **1990**, *112*, 3674.

(11) Betley, T. A.; Peters, J. C. *Angew. Chem. Int. Ed.* **2003**, *42*, 2385.

(12) Lundgren, R. J.; Rankin, M. A.; McDonald, R.; Schatte, G.; Stradiotto, M. *Angew. Chem. Int. Ed.* **2007**, *46*, 4732.

(13) Coppens, P. *X-ray Charge Densities and Chemical Bonding*; Oxford University Press, Inc.: New York, 1997.

(14) Lecomte, C.; Aubert, E.; Legrand, V.; Porcher, F.; Pillet, S.; Guillot, B.; Jelsch, C. *Zeit. Krist.* **2005**, 373-384.

(15) Bader, R. F. W. *Atoms in Molecules: A Quantum Theory*; Oxford University Press: Oxford, U.K., 1990.

(16) Popelier, P. L. A. *Atoms in Molecules: An Introduction*; Prentice Hall: London, 2000.

(17) Matta, C. F.; Boyd, R. J. *The Quantum Theory of Atoms in Molecules: From Solid State to DNA and Drug Design*; Wiley-VCH: Weinheim, 2007.

(18) Stradiotto, M.; Cipot, J.; McDonald, R. *J. Am. Chem. Soc.* **2003**, *125*, 5618.

(19) Cipot, J.; McDonald, R.; Ferguson, M. J.; Schatte, G.; Stradiotto, M. *Organometallics* **2007**, *26*, 594.

(20) Santi, S.; Ceccon, A.; Crociani, L.; Gambaro, A.; Ganis, P.; Tiso, M.; Venzo, A.; Bacchi, A. *Organometallics* **2002**, *21*, 565.

(21) Schumann, H.; Stenzel, O.; Dechert, S.; Girgsdies, F.; Blum, J.; Gelman, D.; Halterman, R. L. *Eur. J. Inorg. Chem.* **2002**, 211.

(22) Rupert, K. C.; Liu, C. C.; Nguyen, T. T.; Whitener, M. A.; Sowa, J. R. Jr. *Organometallics* **2002**, *21*, 144.

(23) Schumann, H.; Stenzel, O.; Dechert, S.; Girgsdies, F.; Halterman, R. L. *Organometallics* **2001**, *20*, 5360.

(24) Schumann, H.; Stenzel, O.; Dechert, S.; Girgsdies, F.; Halterman, R. L. *Organometallics* **2001**, *20*, 2215.

(25) Westcott, S. A.; Kakkar, A. K.; Taylor, N. J.; Roe, D. C.; Marder, T. B. *Can. J. Chem.* **1999**, *77*, 205.

(26) CrysAlis CCD and CrysAlis RED (Versions 1.171.33.13). Oxford Diffraction. 2008. Abingdon, Oxfordshire, England, Oxford Diffraction Ltd.

(27) Blessing, R. H. *J. Appl. Crystallogr.* **1997**, *30*, 421-426.

(28) Sheldrick, G. M. SHELXS97 AND SHELXL97 programs for crystal structure refinement. Germany, University of Gottengen, 1997.

(29) Sheldrick, G. M. *Acta Cryst. A.* **2008**, *64*, 112-122.

(30) Farrugia, L.J. WinGX (Version 1.64.05). J. 1999.

(31) Farrugia, L. J. *J. Appl. Crystallogr.* **1999**, *32*, 837-838.

(32) Hansen, N. K.; Coppens, P. *Acta Cryst.* **1978**, *A34*, 909-921.

(33) Guillot, B.; Viry, L.; Guillot, R.; Lecomte, C.; Jelsch, C. J. *J. App. Cryst.* **2001**, *34*, 214-223.

(34) Jelsch, C.; Guillot, B.; Lagoutte, L.; Lecomte, C. *MoProViewer: a Molecular Viewer Dedicated to Charge Density Analysis. (Poster, French Crystallogr. Assoc. AFC2010 (Strasbourg), 7-10 July 2010). http://www.crm2.uhp-nancy.fr/crm2/ fr/labo/equipes/emqc/.*

(35) Su, Z.; Coppens, P. *Acta Cryst. A.* **1998**, *54*, 646-652.

(36) Macchi, P.; Coppens, P. *Acta Cryst. A* **2001**, *57*, 656-662.

(37) Stewart, R. F.; Davidson, E. R.; Simpson, W. T. *J. Chem. Phys.* **1965**, *42*, 3175-3187.

(38) Volkov, A.; Abramov, Y.; Coppens, P. *Acta Cryst. A* **2001**, *57*, 272-282.

(39) Allen, F. H.; Kennard, O.; Watson, D.; Brammer, L.; Orpen, A.; Taylor, R. *International Tables for Crystallography, Vol. C, Chapter 9.5, pp. 685-706*; Kluwer Academic Publishers: Dordrecht, 1992.

(40) Madsen, A. Ų. *J. Appl. Cryst.* **2006**, *39*, 757-758.

(41) Hirshfeld, F. L. *Acta Cryst. A* **1976**, *32*, 239-244.

(42) Macchi, P.; Proserpio, D. M.; Sironi, A. *J. Am. Chem. Soc.* **1998**, *120*, 1447-1455.

(43) Stash, A.; Tsirelson, V. *J. Appl. Cryst.* **2002**, *35*, 371-373.

(44) Parr, R. G.; Yang, W. *Density-Functional Theory of Atoms and Molecules*; Oxford University Press: Oxford, 1989.

(45) Koch, W.; Holthausen, M. C. *A Chemist's Guide to Density Functional Theory, (Second Edition)*; Wiley-VCH: New York, 2001.

(46) Lee, C.; Yang, W.; Parr, R. *Phys. Rev. B* **1988**, *37*, 785-789.

(47) Becke, A. *J. Chem. Phys.* **1993**, *98*, 5648-5652.

(48) Chesnut, D. B.; Rusiloski, B. E.; Moore, K. D.; Egolf, D. A. *J. Comput. Chem.* **1993**, *14*, 1364-1375.

(49) Chesnut, D. B.; Byrd, E. F. C. *J. Comput. Chem.* **1996**, *17*, 1431-1443.

(50) DiLabio, G. A.; Wright, J. S. *Chem. Phys. Lett.* **1998**, *297*, 181-186.

(51) DiLabio, G. A. *J. Phys. Chem. A* **1999**, *103*, 11414-11424.

(52) Cramer, C. J. *Essentials of Computational Chemistry: Theories and Models*; John Wiley & Sons, Ltd.: New York, 2002.

(53) Jensen, F. *Introduction to Computational Chemistry*; John Wiley and Sons Ltd.: West Sussex (UK), 2007.

(54) Peterson, K. A. F. D.; Dolg, M.; Stoll, H. *J. Chem. Phys.* **2007**, *126*, 124101_1-124101_12.

(55) Prascher, B.; Woon, D.; Peterson, K.; Dunning, T.; Wilson, A. *Theoret. Chem. Acc. (Theoret. Chim. Acta)* **2011**, *128*, 69-82.

(56) Tiana, D.; Francisco, E.; Blanco, M. A.; Martin Pendas, A. *J. Phys. Chem. A* **2009**, *113*, 7963-7971.

(57) Keith, T. A.; Frisch, M. J. *J. Phys. Chem. A* **2011**, 115, 12879-12894.

(58) de Castro, E. V. R.; Jorge, F. E. *J. Chem. Phys.* **1998**, *108*, 5225-5229.

(59) Douglas, M.; Kroll, N. M. *Ann. Phys. (N. Y.)* **1974**, *82*, 89-155.

(60) Hess, B. A. *Phys. Rev. A* **1985**, *32*, 756-763.

(61) Hess, B. A. *Phys. Rev. A* **1986**, *33*, 3742-3748.

(62) Jansen, G.; Hess, B. A. *Phys. Rev. A* **1989**, *39*, 6016-6017.

(63) Frisch, M. J., Trucks, G. W., Schlegel, H. B., Scuseria, G. E., Robb, M. A., Cheeseman, J. R., Scalmani, G., Barone, V., Mennucci, B., Petersson, G. A., Nakatsuji, H., Caricato, M., Li, X., Hratchian, H. P., Izmaylov, A. F., Bloino, J., Zheng, G., Sonnenberg, J. L., Hada, M., Ehara, M., Toyota, K., Fukuda, R., Hasegawa, J., Ishida, M., Nakajima, T., Honda, Y., Kitao, O., Nakai, H., Vreven, T., Montgomery Jr, J. A., Peralta, J. E., Ogliaro, F., Bearpark, M., Heyd, J. J., Brothers, E., Kudin, K. N., Staroverov, V. N., Keith, T., Kobayashi, R., Normand, J., Raghavachari, K., Rendell, A., Burant, J. C., Iyengar, S. S., Tomasi, J., Cossi, M., Rega, N., Millam, J. M., Klene, M., Knox, J. E., Cross, J. B., Bakken, V., Adamo, C., Jaramillo, J., Gomperts, R., Stratmann, R. E., Yazyev, O., Austin, A. J., Cammi, R., Pomelli, C., Ochterski, J. W., Martin, R. L., Morokuma, K., Zakrzewski, V. G., Voth, G. A., Salvador, P., Dannenberg, J. J., Dapprich, S., Daniels, A. D., Farkas, O., Foresman, J. B., Ortiz, J. V., Cioslowski, J., and Fox, D. J. 2010. Gaussian 09, Revision B.01. Wallingford CT, Gaussian Inc.

(64) Keith, T. A. AIMAll (Version 11.05.16, Professional), aim@tkgristmill.com. 2011.

(65) Dunning, T. H.; Peterson, K. A.; Wilson, A. K. *J. Chem. Phys.* **2001**, *114*, 9244-9253.

(66) EMSL Basis Set Exchange *https://bse.pnl.gov/bse/portal*; EMSL-Office of Science: 2011.

(67) Peterson, K. A. *Personal communication*; 2011.

(68) Sparkes, H. A.; Brayshaw, S. K.; Weller, A. S.; Howard, J. A. K. *Acta Cryst. B* **2008**, *64*, 550-557.

(69) Runtz, G. R.; Bader, R. F. W.; Messer, R. R. *Can. J. Chem.* **1977**, *55*, 3040-3045.

(70) Bader, R. F. W. *J. Phys. Chem. A* **1998**, *102*, 7314-7323.

(71) Bader, R. F. W. *J. Phys. Chem. A* **2009**, *113*, 10391-10396.

(72) Fradera, X.; Austen, M. A.; Bader, R. F. W. *J. Phys. Chem. A* **1999**, *103*, 304-314.

(73) Martin Pendas, A.; Francisco, E.; Blanco, M. A.; Gatti, C. *Chem. Eur. J.* **2007**, *13*, 9362-9371.

(74) Bader, R. F. W.; Matta, C. F. *Inorg. Chem.* **2001**, *40*, 5603-5611.

(75) Matta, C. F.; Hernández-Trujillo, J. *J. Phys. Chem. A* **2003**, *107*, 7496-7504 (Correction: J. Phys. Chem A, **2005**, *109*, 10798).

(76) Macchi, P.; Sironi, A. *Coord. Chem. Rev.* **2003**, *238-239*, 383-412.

(77) Matta, C. F.; Hernández-Trujillo, J.; Tang, T. H.; Bader, R. F. W. *Chem. Eur. J.* **2003**, *9*, 1940-1951.

(78) Paul, A. ; Kubicki, M.; Jelsch, C.; Durand, P.; Lecomte, C. *Acta Cryst. B* **2011**, *67*, 365-378.

(79) Hernández-Trujillo, J.; Matta, C. F. *Struct. Chem.* **2007**, *18*, 849-857.

(80) Matta, C. F. Hydrogen-hydrogen bonding: The non-electrostatic limit of closed-shell interaction between two hydrogen atoms. A critical review; In *Hydrogen Bonding - New Insight, (Challenges and Advances in Computational Chemistry and Physics Series)*; Grabowski, S. Ed., ed. Springer: 2006; pp 337-376.

(81) Bakhmutov, V. I. *Dihydrogen Bonds: Principles, Experiments, and Applications*; Wiley-Interscience: New Jersey, 2008.

(82) Farrugia, L. J.; Evans, C.; Lentz, D.; Roemer, M. *J. Am. Chem. Soc.* **2009**, *131*, 1251-1268.

(83) Sparkes, H. A.; Chaplin, A. B.; Weller, A. S.; Howard, J. A. K. *Acta Cryst. B* **2010**, *66*, 503-514.

(84) Cremer, D.; Kraka, E. *Angew. Chem. Int. Ed. Engl.* **1984**, *23*, 627-628.

(85) Rohrmoser, B.; Eickerling, G.; Presnitz, M.; Scherer, W.; Eyert, V.; Hoffmann, R.-D.; Rodewald, U. C.; Vogt, C.; PŲttgen, R. J. *J. Am. Chem. Soc.* **2007**, *129*, 9356-9365.

(86) Dewar, M. J. S. *Bull. Soc. Chim. Fr.* **1951**, *18*, C71-C79.

(87) Chatt, J.; Duncanson, L. A. *J. Chem. Soc.* **1953**, 2939-2947.

(88) Macchi, P.; Sironi, A. Metal involving interactions: From "chemical categories" to QTAIM and backwards; In *The Quantum Theory of Atoms in Molecules: From Solid State to DNA and Drug Design*; Matta, C. F., Boyd, R. J., eds. Wiley-VCH: Weinheim, 2007.

(89) Scherer, W.; Eickerling, G.; Shorokhov, D.; Gullo, E.; McGrady, G. S.; Sirsch, P. *New J. Chem.* **2006**, *30*, 309-312.

(90) Nuss, H. ; Claiser, N.; Pillet, S.; Lugan, N.; Despagnet-Ayoub, E.; Etienne, M.; Lecomte, C. *Dalton Trans.* **2012**, submitted.

(91) Coppens, P.; Iversen, B.; Larsen, F. K. *Coord. Chem. Rev.* **2005**, *249*, 179-195.

(92) Chen, Z.; Wannere, C. S.; Corminboeuf, C.; Puchta, R.; Schleyer, P. v. R. *Chem. Rev.* **2005**, *105*, 3842-3888.

(93) Schleyer P.v-R.; Maerker, C.; Dransfeld, A.; Jiao, H.; Hommes, N. J. R. v. E. *J. Am. Chem. Soc.* **1996**, *118*, 6317-6318.

(94) Ghermani, N.; Bouhmaida, N.; Lecomte, C. *ELECTROS: A Computer Program to Calculate Electrostatic Properties from High Resolution X-ray Diffraction. Internal Report URA CNRS 809, University of Nancy 1, France* **1992**.

(95) Macrae, C. F.; Bruno, I. J.; Chisholm, J. A.; Edgington, P. R.; McCabe, P.; Pidcock, E.; Rodriguez-Monge, L.; Taylor, R.; van de Streek, J.; Wood, P. A. *J. Appl. Cryst.* **2008**, *41*, 466-470.

**Table 1** Main crystallographic features, X-ray diffraction data collection parameters and final results for **1c** and **1z**.[(a)]

| Crystal data | Cationic Complex (1c) | Zwitterionic Complex (1z) |
|---|---|---|
| Chemical formula | $(C_{25}H_{38}NPRh)^+$, $(CF_3SO_3)^-$ | $C_{25}H_{37}NPRh$ |
| Formula weight (g $mol^{-1}$) | 635.53 | 485.46 |
| Cell setting, space group | Monoclinic, $P2_1/n$ | Monoclinic, $P2_1/c$ |
| Temperature (K) | 30 (1) | 30 (1) |
| $a, b, c$ (Å) | 9.9971(1), 20.1773(3), 14.1321(2) | 9.6410(1), 16.8404(1), 14.3917(2) |
| β (°) | 103.452(1) | 109.269(1) |
| $V$ (Å$^3$) | 2772.44(6) | 2205.71(4) |
| $Z$ | 4 | 4 |
| $D_x$ (Mg $m^{-3}$) | 1.523 | 1.462 |
| Radiation type, Wavelength (Å) | Synchrotron, 0.54856 | Synchrotron, 0.54737 |
| μ ($mm^{-1}$) | 0.335 | 0.458 |
| Crystal form, colour | Plate, orange | Plate, brown |
| Crystal size (mm) | 0.130 × 0.120 × 0.100 | 0.125 × 0.125 × 0.100 |
| Diffractometer | Newport-Oxford | Newport-Oxford |
| Data collection method | ω | ω |
| Absorption correction | Empirical (Sortav) | Empirical (Sortav) |
| $T_{min}$, $T_{max}$ | 0.953, 0.988 | 0.934, 0.972 |
| No. of measured, independent and observed reflections ($I > 2\sigma(I)$) | 1 355 281, 57136, 47301 | 812 400, 42449, 37162 |
| $R_{int}$ | 0.068 | 0.058 |
| $\theta_{min}$, $\theta_{max}$ (°) | 1.56, 50.32 | 1.48, 48.38 |
| Sin($\theta_{max}$)/λ (Å$^{-1}$) | 1.403 | 1.366 |
| **Spherical Refinements** | | |
| Refinement on | $F^2$ | $F^2$ |
| $R[F^2 > 2\sigma(F^2)]$, $wR(F^2)$, $S$ | 0.041, 0.119, 1.11 | 0.033, 0.094, 1.12 |
| No. of reflections | 47301 | 37162 |
| No. of parameters | 478 | 401 |
| Weighting scheme | Calculated $w = 1/[\sigma^2(F_{obs}^2) + (0.0900P)^2 + 0.0052P]$ where $P = (F_{obs}^2 + 2F_{cal}^2)/3$ | Calculated $w = 1/[\sigma^2(F_{obs}^2) + (0.0612P)^2 + 0.0294P]$ where $P = (F_{obs}^2 + 2F_{cal}^2)/3$ |
| $(\Delta/\sigma)_{max}$ | 0.01 | 0.004 |
| $\Delta\rho_{max}$, $\Delta\rho_{min}$ (e Å$^{-3}$) | 2.676, –2.750 | 3.879, –2.299 |
| **Multipole Refinements (MoPro refinement method)** | | |
| Refinement on | F | F |
| $R[F > 0\sigma(F)]$, $wR(F)$, $S$ | 0.029, 0.021, 1.97 | 0.026, 0.017, 1.73 |
| No. Data & Restraints | 57136, 84 | 42449, 80 |
| No. of parameters | 1791 | 1490 |
| Ω Weighting scheme | $w = 1/[\sigma^2(F_{obs}^2)$ | $w = 1/[\sigma^2(F_{obs}^2)$ |
| $\Delta\rho_{max}$, $\Delta\rho_{min}$ (e Å$^{-3}$) | 0.113, –0.120 | 0.227, –0.160 |

$R(F) = \Sigma[F_{obs} - k\,|F_{cal}|] / \Sigma F_{obs}$

$wR^2(F) = [\,\Sigma\, w\, [\,F_{obs} - k\,|F_{cal}|\,]^2 / \Sigma\, w\, F_{obs}^2\,]^{1/2}$

$S = [\,\Sigma\, w\, [F_{obs} - |F_{cal}|]^2 / (n-p)\,]^{1/2}$

$n$ is the number of reflections and restraints, and $p$ is the total number of parameters refined

**Table 2** Geometric characteristics of intra- and inter-molecular hydrogen bonds: Distances and angle between donor, hydrogen and oxygen acceptor atoms. Interaction involving the fluorine atoms in **1c** (H···F) are also listed.*

| D—H | ··· | A | D—H (Å) | H···A (Å) | D···A (Å) | D—H···A (degrees) |
|---|---|---|---|---|---|---|
| ***Cationic complex 1c*** | | | | | | |
| C1-H1 | ··· | O2 | 1.083(2) | 2.322(2) | 3.3811(3) | 165(1) |
| C10-H102 | ··· | O2 | 1.066(2) | 2.507(1) | 3.5637(6) | 174(1) |
| C19-H191 | ··· | O2 | 1.092(2) | 2.606(14) | 3.5060(1) | 142(1) |
| C21-H211 | ··· | O2 | 1.063(7) | 2.389(11) | 3.4113(6) | 160(1) |
| C12-H12 | ··· | O1 | 1.099(2) | 2.607(12) | 3.461(1) | 134(1) |
| C15-H151 | ··· | O1 | 1.092(2) | 2.627(13) | 3.649(1) | 155(1) |
| C20-H201 | ··· | O1 | 1.057(2) | 2.534(13) | 3.545(1) | 164(1) |
| C12-H12 | ··· | O3 | 1.099(2) | 2.466(13) | 3.4631(7) | 146.6(9) |
| C9-H9 | ··· | F1 | 1.099(2) | 2.473(5) | 3.509(1) | 160(1) |
| C18-H181 | ··· | F2 | 1.092(2) | 2.556(8) | 3.544(7) | 150(1) |
| ***Zwitterionic complex 1z*** | | | | | | |
| C7-H7 | ··· | C23 | 1.083(3) | 2.804(2) | 3.5412(8) | 125(3) |
| C23-H232 | ··· | C16 | 1.059(3) | 2.843(2) | 3.4250(9) | 123(3) |
| *The C-H…π intermolecular interactions* ***:*** | | | | | | |
| C18-H182 | ··· | C3A | 1.092(3) | 2.587(1) | 3.6449(8) | 163(2) |
| C14-H141 | ··· | C6 | 1.091(3) | 2.723(2) | 3.7853(7) | 164(2) |
| C14-H141 | ··· | C7 | 1.091(3) | 2.754(3) | 3.7761(7) | 156(2) |

---

* In the C18-H182…π interaction, the ring carbon atom closest to the hydrogen H182 is C3A with a distance of 2.587(1) Å and an angle between C18, H182 and C3A of 163(2)°.

The geometric characteristics of the C14-H141…π interactions show that the atoms which are closest from the hydrogen atom H141 are C6 and C7 at respectively 2.723(2) Å and 2.754(3) Å. The atoms C14, H141 and C6 form an angle of 164(2)° while the C14, H141 and C7 angle is 156(2)°.

**Table 3** Bond properties within the rhodium coordination sphere.[(a)]

| Bond | System-Method[(b)] | BL[(c)] | BL-BPL[(d)] | δ(A,B) | $\rho_b$ | $\nabla^2\rho_b$ | $\lambda_1$ | $\lambda_2$ | $\lambda_3$ | $\varepsilon$ | $V_b$ | $G_b$ | $H_b$ | $G_b/\rho$ | $H_b/\rho$ | $\lvert V_b/G_b\rvert$ |
|---|---|---|---|---|---|---|---|---|---|---|---|---|---|---|---|---|
| Rh1–N1 | **C**-Xry | 2.2233(2) | -0.0073 | | 0.078 | 0.26 | -0.09 | -0.08 | 0.43 | 0.07 | -0.10 | 0.08 | -0.02 | 1.03 | -0.26 | 1.25 |
| | **C**-sp | 2.2234 | 0.0016 | 0.508 | 0.075 | 0.27 | -0.09 | -0.06 | 0.42 | 0.38 | -0.10 | 0.08 | -0.02 | 1.11 | -0.23 | 1.20 |
| | **C**-opt | 2.2699 | 0.0019 | 0.483 | 0.068 | 0.24 | -0.08 | -0.05 | 0.37 | 0.40 | -0.09 | 0.07 | -0.01 | 1.08 | -0.20 | 1.19 |
| | **Z**-Xry | 2.2363(2) | -0.0062 | | 0.075 | 0.28 | -0.10 | -0.07 | 0.45 | 0.42 | -0.10 | 0.09 | -0.01 | 1.20 | -0.13 | 1.11 |
| | **Z**-sp | 2.2363 | 0.0009 | 0.509 | 0.075 | 0.25 | -0.09 | -0.06 | 0.40 | 0.40 | -0.10 | 0.08 | -0.02 | 1.05 | -0.23 | 1.22 |
| | **Z**-opt | 2.2719 | 0.0007 | 0.494 | 0.069 | 0.23 | -0.08 | -0.06 | 0.37 | 0.43 | -0.09 | 0.07 | -0.01 | 1.03 | -0.21 | 1.20 |
| Rh1–P1 | **C**-Xry | 2.3079(1) | -0.0627 | | 0.095 | 0.08 | -0.11 | -0.08 | 0.27 | 0.44 | -0.12 | 0.07 | -0.05 | 0.73 | -0.52 | 1.71 |
| | **C**-sp | 2.3079 | 0.0035 | 0.886 | 0.103 | 0.12 | -0.10 | -0.08 | 0.30 | 0.14 | -0.11 | 0.07 | -0.04 | 0.68 | -0.40 | 1.58 |
| | **C**-opt | 2.3365 | 0.0037 | 0.878 | 0.098 | 0.12 | -0.09 | -0.08 | 0.28 | 0.14 | -0.10 | 0.07 | -0.04 | 0.67 | -0.38 | 1.56 |
| | **Z**-Xry | 2.3085(8) | -0.0196 | | 0.103 | 0.16 | -0.11 | -0.10 | 0.36 | 0.11 | -0.14 | 0.09 | -0.05 | 0.87 | -0.48 | 1.56 |
| | **Z**-sp | 2.3085 | 0.0022 | 0.876 | 0.106 | 0.09 | -0.10 | -0.09 | 0.28 | 0.13 | -0.11 | 0.07 | -0.04 | 0.62 | -0.41 | 1.66 |
| | **Z**-opt | 2.3702 | 0.0031 | 0.839 | 0.095 | 0.09 | -0.09 | -0.08 | 0.26 | 0.14 | -0.09 | 0.06 | -0.04 | 0.60 | -0.37 | 1.61 |
| Rh1–C12 | **C**-Xry | 2.2250(2) | -0.0166 | | 0.075 | 0.21 | -0.08 | -0.02 | 0.31 | 2.73 | -0.09 | 0.07 | -0.02 | 0.93 | -0.27 | 1.29 |
| | **C**-sp | 2.2251 | 0.0404 | 0.545 | 0.082 | 0.17 | -0.08 | -0.04 | 0.30 | 0.87 | -0.09 | 0.07 | -0.02 | 0.80 | -0.26 | 1.33 |
| | **C**-opt | 2.2535 | 0.0470 | 0.520 | 0.077 | 0.17 | -0.07 | -0.04 | 0.28 | 0.86 | -0.08 | 0.06 | -0.02 | 0.79 | -0.25 | 1.31 |
| | **Z**-Xry | 2.2365(3) | -0.2541 | | 0.078 | 0.25 | -0.08 | -0.02 | 0.35 | 4.24 | -0.10 | 0.08 | -0.02 | 1.03 | -0.26 | 1.25 |
| | **Z**-sp | 2.2365 | 0.0343 | 0.523 | 0.079 | 0.19 | -0.07 | -0.04 | 0.29 | 0.92 | -0.09 | 0.07 | -0.02 | 0.85 | -0.26 | 1.30 |
| | **Z**-opt | 2.2450 | 0.0313 | 0.531 | 0.078 | 0.18 | -0.07 | -0.04 | 0.29 | 0.75 | -0.08 | 0.06 | -0.02 | 0.82 | -0.25 | 1.31 |
| Rh1–C13[(e)] | **C**-Xry | 2.2673(2) | -0.0027 | | 0.073 | 0.20 | -0.08 | 0.00 | 0.28 | 18.10 | -0.09 | 0.07 | -0.02 | 0.95 | -0.27 | 1.29 |
| | **C**-sp | 2.2672 | | 0.509 | | | | | | | | | | | | |
| | **C**-opt | 2.3071 | | 0.480 | | | | | | | | | | | | |
| | **Z**-Xry | 2.2725(3) | | | | | | | | | | | | | | |
| | **Z**-sp | 2.2725 | | 0.503 | | | | | | | | | | | | |
| | **Z**-opt | 2.2921 | | 0.503 | | | | | | | | | | | | |
| Rh1–C16 | **C**-Xry | 2.1717(2) | -0.0280 | | 0.096 | 0.21 | -0.13 | -0.03 | 0.37 | 2.86 | -0.13 | 0.09 | -0.04 | 0.93 | -0.41 | 1.44 |
| | **C**-sp | 2.1717 | 0.0308 | 0.660 | 0.094 | 0.20 | -0.09 | -0.03 | 0.32 | 1.78 | -0.11 | 0.08 | -0.03 | 0.82 | -0.30 | 1.37 |
| | **C**-opt | 2.1871 | 0.0431 | 0.651 | 0.091 | 0.20 | -0.09 | -0.03 | 0.31 | 2.52 | -0.10 | 0.08 | -0.03 | 0.84 | -0.29 | 1.35 |
| | **Z**-Xry | 2.1193(2) | -0.0345 | | 0.097 | 0.26 | -0.10 | -0.00 | 0.37 | 23.80 | -0.14 | 0.10 | -0.04 | 1.03 | -0.41 | 1.40 |
| | **Z**-sp | 2.1193 | 0.0133 | 0.710 | 0.104 | 0.19 | -0.11 | -0.07 | 0.37 | 0.65 | -0.12 | 0.08 | -0.03 | 0.79 | -0.33 | 1.42 |
| | **Z**-opt | 2.1526 | 0.0198 | 0.687 | 0.097 | 0.19 | -0.10 | -0.05 | 0.34 | 0.87 | -0.11 | 0.08 | -0.03 | 0.79 | -0.31 | 1.39 |
| Rh1–C17 | **C**-Xry | 2.1347(2) | -0.0352 | | 0.098 | 0.25 | -0.10 | -0.05 | 0.40 | 0.92 | -0.14 | 0.10 | -0.04 | 1.02 | -0.41 | 1.40 |
| | **C**-sp | 2.1347 | 0.0186 | 0.689 | 0.101 | 0.17 | -0.11 | -0.07 | 0.35 | 0.60 | -0.11 | 0.07 | -0.03 | 0.74 | -0.32 | 1.43 |
| | **C**-opt | 2.1478 | 0.0227 | 0.679 | 0.098 | 0.17 | -0.11 | -0.06 | 0.34 | 0.65 | -0.10 | 0.07 | -0.03 | 0.74 | -0.31 | 1.42 |
| | **Z**-Xry | 2.1272(3) | -0.0482 | | 0.099 | 0.22 | -0.12 | -0.04 | 0.38 | 1.99 | -0.14 | 0.10 | -0.04 | 1.01 | -0.40 | 1.40 |
| | **Z**-sp | 2.1271 | 0.0153 | 0.697 | 0.102 | 0.19 | -0.11 | -0.06 | 0.36 | 0.77 | -0.11 | 0.08 | -0.03 | 0.79 | -0.33 | 1.41 |
| | **Z**-opt | 2.1463 | 0.0175 | 0.685 | 0.098 | 0.18 | -0.10 | -0.06 | 0.35 | 0.74 | -0.11 | 0.08 | -0.03 | 0.78 | -0.31 | 1.40 |
| N1–C2 | **C**-Xry | 1.4624(2) | -0.0061 | | 0.263 | -0.44 | -0.61 | -0.49 | 0.66 | 0.23 | -0.58 | 0.24 | -0.35 | 0.91 | -1.33 | 2.42 |
| | **C**-sp | 1.4625 | 0.0004 | 0.962 | 0.264 | -0.56 | -0.52 | -0.51 | 0.47 | 0.02 | -0.35 | 0.10 | -0.24 | 0.40 | -0.93 | 3.33 |
| | **C**-opt | 1.4598 | 0.0004 | 0.963 | 0.265 | -0.56 | -0.52 | -0.51 | 0.47 | 0.01 | -0.35 | 0.11 | -0.25 | 0.40 | -0.93 | 3.33 |
| | **Z**-Xry | 1.4653(3) | -0.0069 | | 0.279 | -0.69 | -0.68 | -0.57 | 0.56 | 0.21 | -0.63 | 0.23 | -0.40 | 0.82 | -1.43 | 2.74 |
| | **Z**-sp | 1.4653 | 0.0001 | 0.925 | 0.256 | -0.55 | -0.50 | -0.48 | 0.42 | 0.04 | -0.37 | 0.11 | -0.25 | 0.44 | -0.99 | 3.22 |
| | **Z**-opt | 1.4727 | 0.0001 | 0.925 | 0.252 | -0.53 | -0.49 | -0.47 | 0.42 | 0.04 | -0.35 | 0.11 | -0.24 | 0.43 | -0.96 | 3.22 |
| P1–C3 | **C**-Xry | 1.8117(2) | -0.0097 | | 0.177 | -0.23 | -0.25 | -0.18 | 0.20 | 0.35 | -0.30 | 0.12 | -0.18 | 0.68 | -1.02 | 2.50 |
| | **C**-sp | 1.8117 | 0.0012 | 0.760 | 0.166 | -0.12 | -0.23 | -0.22 | 0.34 | 0.04 | -0.29 | 0.13 | -0.16 | 0.79 | -0.97 | 2.23 |
| | **C**-opt | 1.8163 | 0.0010 | 0.774 | 0.166 | -0.13 | -0.23 | -0.22 | 0.32 | 0.03 | -0.29 | 0.13 | -0.16 | 0.77 | -0.97 | 2.26 |
| | **Z**-Xry | 1.7533(2) | -0.0254 | | 0.163 | -0.10 | -0.21 | -0.15 | 0.26 | 0.45 | -0.27 | 0.12 | -0.15 | 0.73 | -0.92 | 2.25 |

| Bond | System-Method[(b)] | BL[(c)] | BL-BPL[(d)] | δ(A,B) | $\rho_b$ | $\nabla^2\rho_b$ | $\lambda_1$ | $\lambda_2$ | $\lambda_3$ | $\varepsilon$ | $V_b$ | $G_b$ | $H_b$ | $G_b/\rho$ | $H_b/\rho$ | $\lvert V_b/G_b \rvert$ |
|---|---|---|---|---|---|---|---|---|---|---|---|---|---|---|---|---|
| | **Z**-sp | 1.7533 | 0.0008 | 0.837 | 0.182 | -0.10 | -0.26 | -0.24 | 0.40 | 0.10 | -0.34 | 0.16 | -0.18 | 0.88 | -1.01 | 2.15 |
| | **Z**-opt | 1.7522 | 0.0008 | 0.866 | 0.182 | -0.10 | -0.26 | -0.24 | 0.40 | 0.11 | -0.34 | 0.16 | -0.18 | 0.88 | -1.01 | 2.16 |
| C12–C13 | **C**-Xry | 1.3911(3) | -0.0512 | | 0.312 | -0.74 | -0.66 | -0.54 | 0.46 | 0.22 | -0.76 | 0.29 | -0.47 | 0.93 | -1.51 | 2.62 |
| | **C**-sp | 1.3912 | 0.0019 | 1.393 | 0.319 | -1.00 | -0.71 | -0.56 | 0.27 | 0.27 | -0.48 | 0.11 | -0.37 | 0.36 | -1.15 | 4.19 |
| | **C**-opt | 1.3756 | 0.0018 | 1.416 | 0.330 | -1.08 | -0.74 | -0.59 | 0.25 | 0.26 | -0.51 | 0.12 | -0.39 | 0.36 | -1.18 | 4.25 |
| | **Z**-Xry | 1.3785(4) | -0.0053 | | 0.326 | -0.77 | -0.69 | -0.53 | 0.45 | 0.31 | -0.82 | 0.31 | -0.51 | 0.95 | -1.57 | 2.65 |
| | **Z**-sp | 1.3784 | 0.0016 | 1.412 | 0.327 | -1.06 | -0.73 | -0.57 | 0.25 | 0.28 | -0.50 | 0.12 | -0.38 | 0.37 | -1.18 | 4.20 |
| | **Z**-opt | 1.3772 | 0.0017 | 1.408 | 0.328 | -1.07 | -0.74 | -0.58 | 0.25 | 0.27 | -0.51 | 0.12 | -0.39 | 0.37 | -1.18 | 4.22 |
| C16–C17 | **C**-Xry | 1.4129(3) | -0.0100 | | 0.293 | -0.54 | -0.56 | -0.46 | 0.48 | 0.23 | -0.70 | 0.28 | -0.42 | 0.95 | -1.43 | 2.50 |
| | **C**-sp | 1.4131 | 0.0025 | 1.283 | 0.306 | -0.92 | -0.67 | -0.54 | 0.29 | 0.24 | -0.44 | 0.11 | -0.34 | 0.34 | -1.09 | 4.19 |
| | **C**-opt | 1.3969 | 0.0025 | 1.294 | 0.316 | -1.00 | -0.70 | -0.57 | 0.27 | 0.23 | -0.47 | 0.11 | -0.36 | 0.35 | -1.13 | 4.26 |
| | **Z**-Xry | 1.4097(4) | -0.0085 | | 0.311 | -0.70 | -0.62 | -0.52 | 0.44 | 0.21 | -0.76 | 0.29 | -0.47 | 0.93 | -1.51 | 2.62 |
| | **Z**-sp | 1.4097 | 0.0026 | 1.265 | 0.307 | -0.93 | -0.67 | -0.54 | 0.29 | 0.25 | -0.45 | 0.11 | -0.34 | 0.35 | -1.10 | 4.17 |
| | **Z**-opt | 1.4002 | 0.0026 | 1.282 | 0.313 | -0.97 | -0.69 | -0.56 | 0.28 | 0.25 | -0.46 | 0.11 | -0.35 | 0.35 | -1.12 | 4.23 |
| C2–C3 | **C**-Xry | 1.3643(3) | -0.0050 | | 0.309 | -0.86 | -0.72 | -0.58 | 0.44 | 0.24 | -0.74 | 0.26 | -0.48 | 0.84 | -1.56 | 2.85 |
| | **C**-sp | 1.3641 | 0.0005 | 1.604 | 0.325 | -0.79 | -0.68 | -0.50 | 0.39 | 0.35 | -0.45 | 0.13 | -0.32 | 0.39 | -0.99 | 3.57 |
| | **C**-opt | 1.3568 | 0.0006 | 1.612 | 0.329 | -0.81 | -0.69 | -0.51 | 0.39 | 0.35 | -0.46 | 0.13 | -0.33 | 0.39 | -1.00 | 3.58 |
| | **Z**-Xry | 1.4196(4) | -0.0073 | | 0.316 | -0.83 | -0.75 | -0.54 | 0.46 | 0.38 | -0.77 | 0.28 | -0.49 | 0.88 | -1.55 | 2.75 |
| | **Z**-sp | 1.4196 | 0.0013 | 1.259 | 0.291 | -0.66 | -0.58 | -0.46 | 0.38 | 0.27 | -0.36 | 0.10 | -0.26 | 0.34 | -0.90 | 3.69 |
| | **Z**-opt | 1.4289 | 0.0014 | 1.253 | 0.286 | -0.64 | -0.57 | -0.45 | 0.38 | 0.27 | -0.35 | 0.09 | -0.25 | 0.33 | -0.89 | 3.69 |

**(a)** All dimensioned quantities are in atomic units (au) except distances which are in Angstroms (Å). δ(*A*.*B*) is the delocalization index between atoms *A* and *B* and is a dimensionless. **(b)** "**C-**" refers to the cationic species (*i.e.* complex **1c**) and "**Z-**" refers to the zwitterionic species (*i.e.* complex **1z**). "Xry" refer to the experimental X-ray results. "sp" refers to the theoretical results obtained from a single point calculation at the experimental geometry and "opt" refers to theoretical results obtained after a full geometry optimization starting from the experimental geometry. **(c)** BL = geometric bond length (internuclear distance). **(d)** BL-BPL = geometric bond length minus the bond path length. **(e)** This bond path is found only in the experimental density of the **1c**.

**Table 4** Basic atomic and group properties in **1c** and **1z**.[(a)]

| **Atom or group** | **System-method[(b)]** | **Cation (1c)** | | | | **Zwitterion (1z)** | | | |
|---|---|---|---|---|---|---|---|---|---|
| | | $q(\Omega)$ | $N(\Omega)$ | Vol(Ω) | $E(\Omega)$ | $q(\Omega)$ | $N(\Omega)$ | Vol(Ω) | $E(\Omega)$ |
| Rh1 | Xry | 0.290 | 44.710 | 125.1 | | 0.295 | 44.705 | 125.3 | |
| | Sp | 0.361 | 44.639 | 127.1 | | 0.362 | 44.638 | 131.7 | |
| | Opt | 0.353 | 44.647 | 132.5 | -42.72191 | 0.369 | 44.631 | 136.7 | -42.68391 |
| ***Atoms bonded to Rh1*** | | | | | | | | | |
| P1 | Xry | 1.188 | 13.812 | 83.4 | | 1.208 | 13.792 | 78.6 | |
| | Sp | 1.664 | 13.336 | 72.0 | | 1.802 | 13.198 | 67.2 | |
| | Opt | 1.580 | 13.420 | 76.4 | -358.76333 | 1.696 | 13.304 | 73.7 | -358.67119 |
| N1 | Xry | -0.655 | 7.655 | 58.1 | | -0.810 | 7.810 | 57.1 | |
| | Sp | -0.900 | 7.900 | 58.3 | | -0.923 | 7.923 | 57.8 | |
| | Opt | -0.910 | 7.910 | 59.2 | -57.77100 | -0.916 | 7.916 | 58.8 | -57.76794 |
| C12 | Xry | -0.158 | 6.158 | 65.2 | | -0.157 | 6.157 | 63.1 | |
| | sp | -0.106 | 6.106 | 63.2 | | -0.121 | 6.121 | 65.9 | |
| | opt | -0.102 | 6.102 | 62.9 | -39.99436 | -0.115 | 6.115 | 65.9 | -39.98371 |
| C13 | Xry | -0.103 | 6.103 | 59.1 | | -0.224 | 6.224 | 59.8 | |
| | sp | -0.130 | 6.130 | 66.5 | | -0.116 | 6.116 | 63.9 | |
| | opt | -0.118 | 6.118 | 65.8 | -39.98435 | -0.108 | 6.108 | 63.2 | -39.99167 |
| C16 | Xry | -0.380 | 6.380 | 68.6 | | -0.222 | 6.222 | 63.5 | |
| | sp | -0.116 | 6.116 | 64.0 | | -0.108 | 6.108 | 62.2 | |
| | opt | -0.103 | 6.103 | 63.0 | -39.96546 | -0.102 | 6.102 | 62.9 | -39.96419 |
| C17 | Xry | -0.239 | 6.239 | 68.2 | | -0.336 | 6.336 | 67.8 | |
| | sp | -0.102 | 6.102 | 62.2 | | -0.110 | 6.110 | 60.5 | |
| | opt | -0.095 | 6.095 | 61.6 | -39.98477 | -0.100 | 6.100 | 61.1 | -39.98305 |
| ***Groups[(c)]*** | | | | | | | | | |
| Indene/indenide | Xry | 0.170 | 59.830 | 957.8 | | -0.754 | 59.752 | 943.5 | |
| | Sp | -0.197 | 60.197 | 952.9 | | -0.924 | 59.924 | 960.1 | |
| | Opt | -0.185 | 60.185 | 956.2 | -363.54921 | -0.918 | 59.918 | 968.9 | -363.09463 |
| COD | Xry | -1.324 | 61.324 | 1113.8 | | -0.410 | 60.409 | 1026.8 | |
| | Sp | 0.071 | 59.929 | 1040.8 | | -0.062 | 60.062 | 1039.2 | |
| | Opt | 0.092 | 59.908 | 1042.6 | -327.26702 | -0.052 | 60.052 | 1048.6 | -327.31458 |
| $R_N$ | Xry | 0.286 | 24.714 | 483.8 | | -0.105 | 25.104 | 490.8 | |
| | sp | -0.167 | 25.167 | 443.5 | | -0.255 | 25.255 | 445.9 | |
| | opt | -0.176 | 25.176 | 455.8 | -141.10724 | -0.252 | 25.252 | 457.7 | -141.14259 |
| $R_P$ | Xry | 1.800 | 63.200 | 1154.5 | | 0.997 | 64.004 | 1123.6 | |
| | sp | 0.931 | 64.069 | 1092.4 | | 0.881 | 64.119 | 1083.1 | |
| | opt | 0.916 | 64.084 | 1124.9 | -607.25375 | 0.855 | 64.145 | 1128.2 | -607.22854 |
| ***SUM[(d)]*** | | | | | | | | | |
| | Xry | 1.190 | 253.810 | 3843.8 | | 0.023 | 253.974 | 3710.0 | |
| | sp | 0.999 | 254.001 | 3656.7 | | 0.002 | 253.998 | 3659.9 | |
| | opt | 1.000 | 254.000 | 3712.0 | -1481.89913 | 0.003 | 253.997 | 3740.1 | -1481.46426 |
| ***Counterion*** | Xry | -0.702 | 73.702 | 832.3 | | | | | |
| ***Cation+counterion*** | Xry | 0.488 | 327.512 | 4676.1 | | | | | |

**(a)** All dimensioned quantities are in atomic units (au). **(b)** "Xry" = experimental X-ray results, "sp" = theoretical results obtained from a single point calculation at the experimental geometry, and "opt" = results from theory after geometry optimization. **(c)** The groups includes the following atoms: Indene(in **1c**)/indenide(in **1z**) = (C1, C2, C3, C3A, C4, C5, C6, C7, C7A, H1, (H2 in **1c** only), H4, H5, H6, H7); COD = (C12, C13, C14, C15, C16, C17, C18, C19, H12, H13, H141, H142, H151, H152, H16, H17, H181, H182, H191, H192); $R_N$ = (N1, C10, C11, H101, H102, H103, H111, H112, H113); and $R_P$ = (P1, C20, C21, C9, C22, C23, H8, H201, H202, H203, H211, H212, H213, H9, H221, H222, H223, H231, H232, H233). **(d)** The sum over the experimental atomic properties in the case of the **1c** is that on all the atoms of the cationic species without the counterion.

# FIGURE CAPTIONS

**Chart 1**
Cationic (**1c**) and formally zwitterionic (**1z**) Rh(I) complexes featured in this study.

**Fig. 1**
The experimental geometry labelled with the numbering scheme of the two Rh complexes, the cation **1c** (top) and the zwitterion **1z** (bottom). Hydrogen atoms are removed for clarity (only H1 and H2 hydrogen atoms are shown to distinguish **1c** from **1z**). The ORTEP 50% thermal ellipsoids are shown for all non-hydrogen atoms. (Colour scheme: Rh = dark green, P = orange, N = dark blue, C = dark gray, and H = light gray).

**Fig. 2**
A representation of the crystal packing of the two complexes along with the corresponding unit cell. Note that the crystal of the cationic complex includes a counterion. Weak inter-molecular interactions are indicated by red dotted lines. (The colour scheme is the same as in **Fig. 1**, but in addition, the colour scheme of the atoms in the counterion is: O = red, F = light green, and S = yellow). **(TOP)** The crystal packing of the **1c** complex is viewed along the ***a*** axis showing the alternating $(C_{25}H_{38}NPRh)^+$ and $(CF_3SO_3)^-$ moities. **(BOTTOM)** View along the ***a*** axis of the crystal packing of the **1z** complex. The views were drawn using the program Mercury.[95]

**Fig. 3**
A representation of the molecular graphs of the two complexes obtained from the theoretically-calculated electron density at the fully optimized geometry. **(a)** The molecular graph of **1c** (without the counterion), **(b)** the corresponding graphs of **1z**. The lines linking the nuclei are the bond paths. The bond paths corresponding to strong interactions ($\rho_b \geq 0.05$ au) are drawn as solid gray lines while those corresponding to weak bonding interaction ($\rho_b < 0.05$ au) are depicted as dotted gray lines. The positions of atomic nuclei are indicated by small spheres following the same colour code as that adopted in **Fig. 1**. In addition, bond critical points (BCP) are indicated by small red spheres, ring critical points (RCP) by small green spheres, and cage critical points (CCP) by small blue spheres. (The corresponding molecular graphs obtained from the experimental densities and from the theoretically calculated at the experimental geometries can be found in the Supplementary Information **Fig. S2**).

**Fig. 4**
**(a)** Static experimental deformation density map for **1z** calculated in the plane Rh1-P1-N1. Contours are depicted at 0.05 e/Å$^3$ (*ca.* 0.007 au) level with positive contours as solid red lines, negative contours as solid blue lines, and the zero level is the faint yellow lines. **(b)** Negative laplacian of the experimental electron density for **1z** in the same plane as **(a)**. Positive contours are red lines, negative contours are blue lines.

**Fig. 5**

Maps of the laplacian in the plane Rh1–C16–C17 obtained from the single-point "sp" calculation at the experimental geometry: Top **C**-sp, bottom **Z**-sp. Positive contours are solid red lines, negative contours as dashed blue lines. The lines linking the nuclear positions are the bond paths, atoms surrounded by a diffuse blue halo are slightly out of the plane of the figure. Only those bond paths trajectories that lie on the plane of the figure are plotted, those out of the plane are omitted. Red dots indicate the position of the bond critical points (BCP) and the green dots the location of the ring critical point (RCP).

**Fig. 6**

Group properties (*P*) of complexes **1c** (top) and their changes ($\Delta P = P(\mathbf{1z}) - P(\mathbf{1c})$) in **1z** (bottom). Charges (*q*) and volumes (Vol) are given in atomic units and energies (*E*) in kcal/mol shown.

**Fig. 7**

Calculated molecular electrostatic potential (ESP) of the two complexes: Two isosurfaces (of magnitudes 0.100 and 0.015 au) showing that the similarity of form of the ESP around the two faces of the catalytic center carries to more than one value of the ESP. On the left is a representation of the molecular geometry in the orientation used to generate the corresponding potential on the right. Red = positive ESP, violet = negative ESP. **(a)** and **(b)** are orientation where the aromatic ring is on the left of the figure, whil;e **(c)** and **(d)** are rotated (roughly) by 180° to show the "back" of the molecule (the aromatic system is on the right of the figure).

**Fig. 8**

Experimentally-determined molecular electrostatic potential (ESP) at an isosurface with $|V(\mathbf{r})| = 0.05$ au that shows the similarity of the form of the ESP around the rhodium atom. (Red = negative ESP, blue = positive ESP).

**Fig. 9**

Molecular electrostatic potential (ESP) nodal surfaces ($V(\mathbf{r}) = 0.000$ au) of the **1z** complex. The nodal surface partitions the complex into a region of negative ESP from the side of the aromatic system and a region of positive ESP surrounding the catalytic center that has a topography similar to that of this region in **1c**.

**Fig. 10**

Calculated molecular electrostatic potential (ESP), $V(\mathbf{r})$, in transparent envelopes, for a truncated model of **1c** (top) and **1z** (bottom) (truncated in that the ter-butyl groups attaced to the P atom are replaced by methyls). The red and blue envelopes represent positive and negative potentials, respectively, while darker surface (in **1z**) that surrounds the aromatic ring and splits the molecule into the aromatic side (left) and rhodium side (right) is the nodal surface separating the regions of positive and negative ESP. The inner solid golden surface isosurface of $\rho(\mathbf{r}) = 0.1$ au is a high electron density envelope in the region close to the nuclear framework of the complexes. The ESP of **1c** (top) is clearly positive everywhere (up to the chosen isosurface) with a depression near the aromatic ring. The ESP of **1z**, however, zwitterionic is partitioned by the nodal surface into teo contiguous regions of positive and negative values, the latter region exhibiting an increasingly more negative values the closer the isosurface is to aromatic ring (the inner dark envelope of $V(\mathbf{r}) = -0.05$ au).

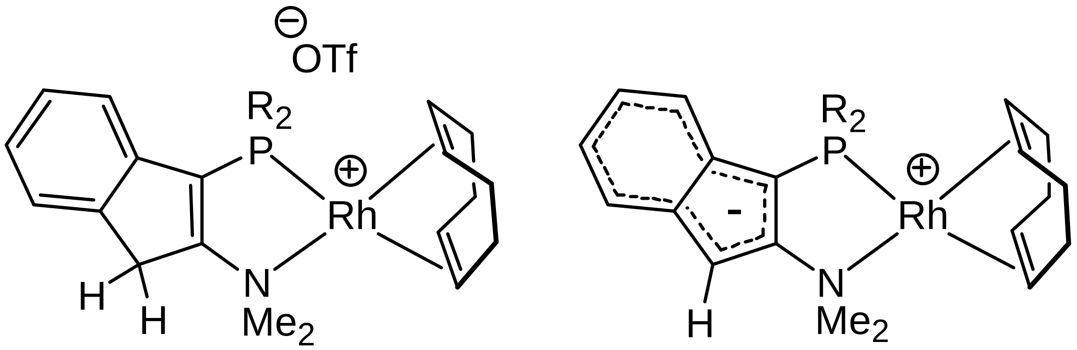

**cationic**

**1c**OTf, R = iPr
**1c'**OTf, R = Me

**zwitterionic**

**1z**, R = iPr
**1z'**, R = Me

**Chart 1**
Cationic (**1c**) and formally zwitterionic (**1z**) Rh(I) complexes featured in this study.

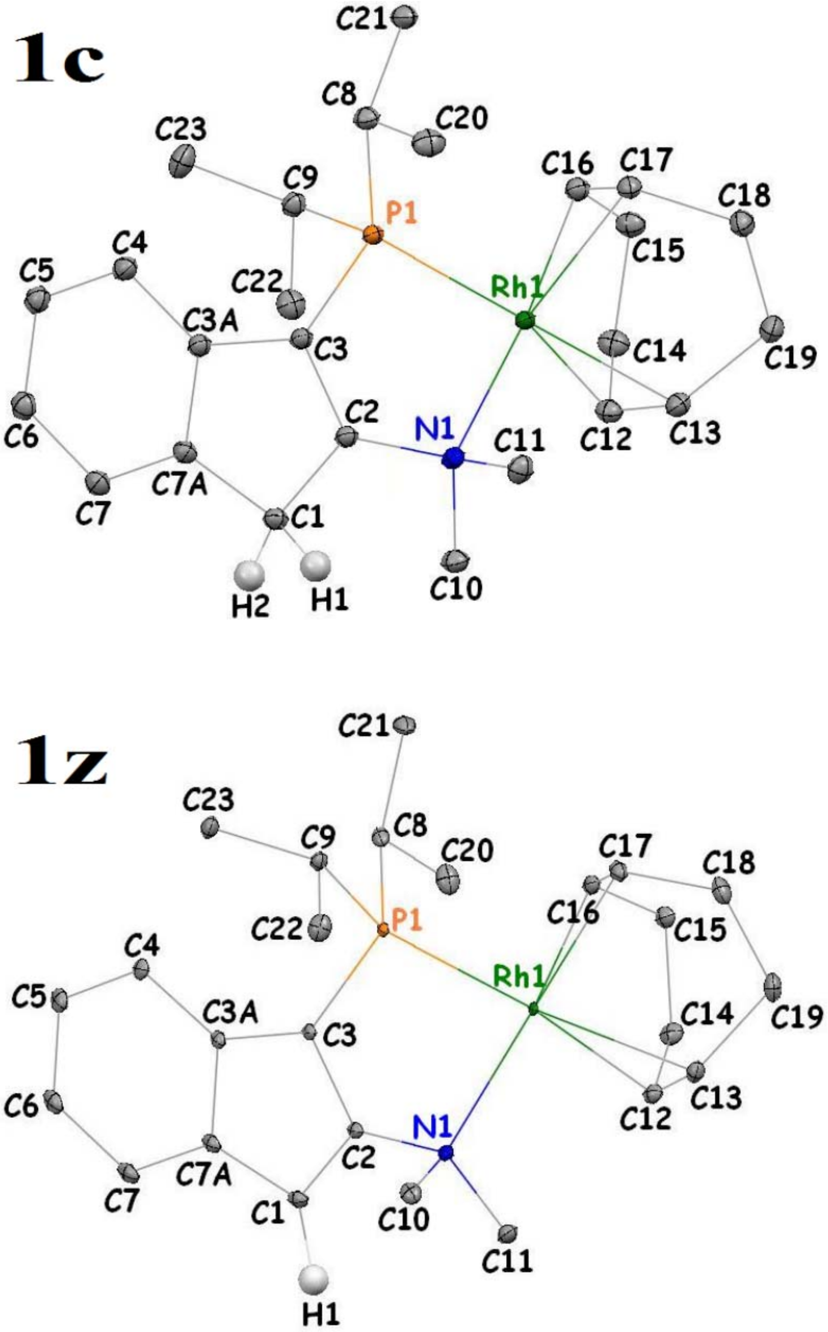

**Fig. 1**
The experimental geometry labelled with the numbering scheme of the two Rh complexes, the cation **1c** (top) and the zwitterion **1z** (bottom). Hydrogen atoms are removed for clarity (only H1 and H2 hydrogen atoms are shown to distinguish **1c** from **1z**). The ORTEP 50% thermal ellipsoids are shown for all non-hydrogen atoms. (Colour scheme: Rh = dark green, P = orange, N = dark blue, C = dark gray, and H = light gray).

Cation (**1c**) with the counterion

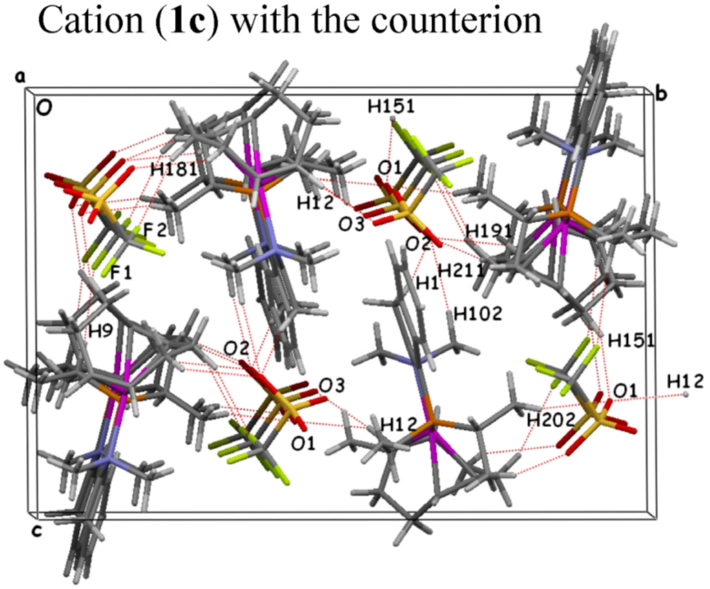

Zwitterion (**1z**)

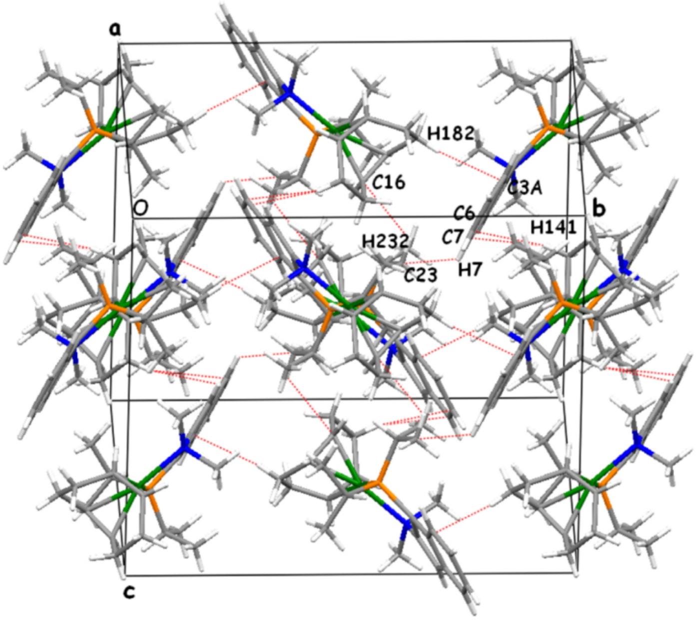

**Fig. 2**

A representation of the crystal packing of the two complexes along with the corresponding unit cell. Note that the crystal of the cationic complex includes a counterion. Weak inter-molecular interactions are indicated by red dotted lines. (The colour scheme is the same as in **Fig. 1**, but in addition, the colour scheme of the atoms in the counterion is: O = red, F = light green, and S = yellow). **(TOP)** The crystal packing of the **1c** complex is viewed along the ***a*** axis showing the alternating $(C_{25}H_{38}NPRh)^{+}$ and $(CF_3SO_3)^{-}$ moities. **(BOTTOM)** View along the ***a*** axis of the crystal packing of the **1z** complex. The views were drawn using the program Mercury.[90]

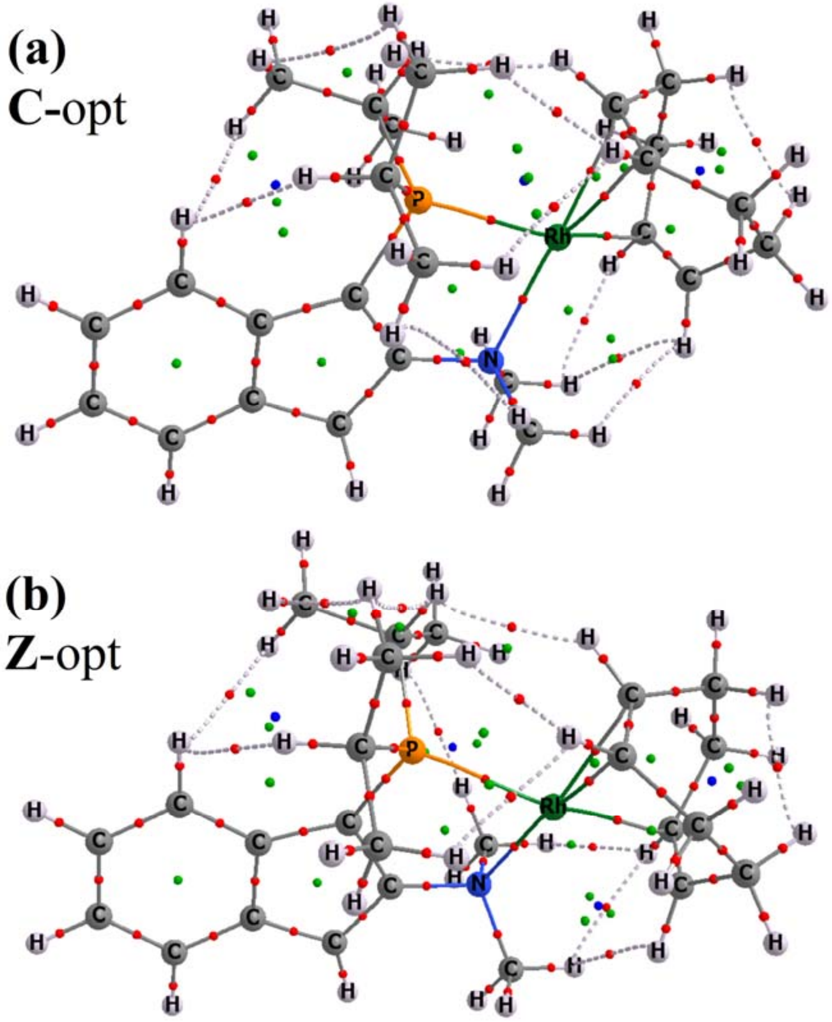

**Fig. 3**
A representation of the molecular graphs of the two complexes obtained from the theoretically-calculated electron density at the fully optimized geometry. **(a)** The molecular graph of **1c** (without the counterion), **(b)** the corresponding graphs of **1z**. The lines linking the nuclei are the bond paths. The bond paths corresponding to strong interactions ($\rho_b \geq 0.05$ au) are drawn as solid gray lines while those corresponding to weak bonding interaction ($\rho_b < 0.05$ au) are depicted as dotted gray lines. The positions of atomic nuclei are indicated by small spheres following the same colour code as that adopted in **Fig. 1**. In addition, bond critical points (BCP) are indicated by small red spheres, ring critical points (RCP) by small green spheres, and cage critical points (CCP) by small blue spheres. (The corresponding molecular graphs obtained from the experimental densities and from the theoretically calculated at the experimental geometries can be found in the Supplementary Information **Fig. S2**).

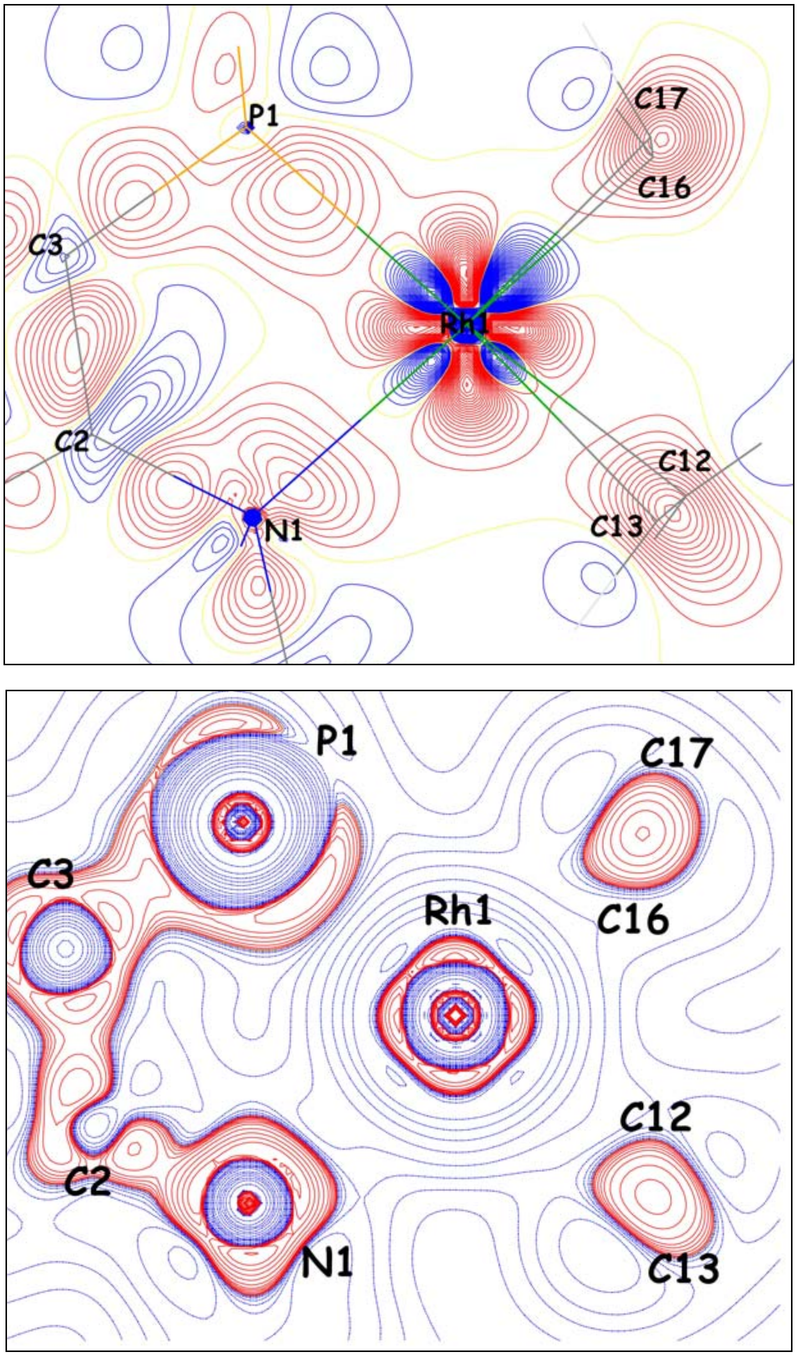

**Fig**. **4**
**(a)** Static experimental deformation density map for **1z** calculated in the plane Rh1–P1–N1. Contours are depicted at 0.05 e/Å$^3$ (*ca.* 0.007 au) level with positive contours as solid red lines, negative contours as solid blue lines, and the zero level is the faint yellow lines. **(b)** Negative laplacian of the experimental electron density for **1z** in the same plane as **(a)**. Positive contours are red lines, negative contours are blue lines.

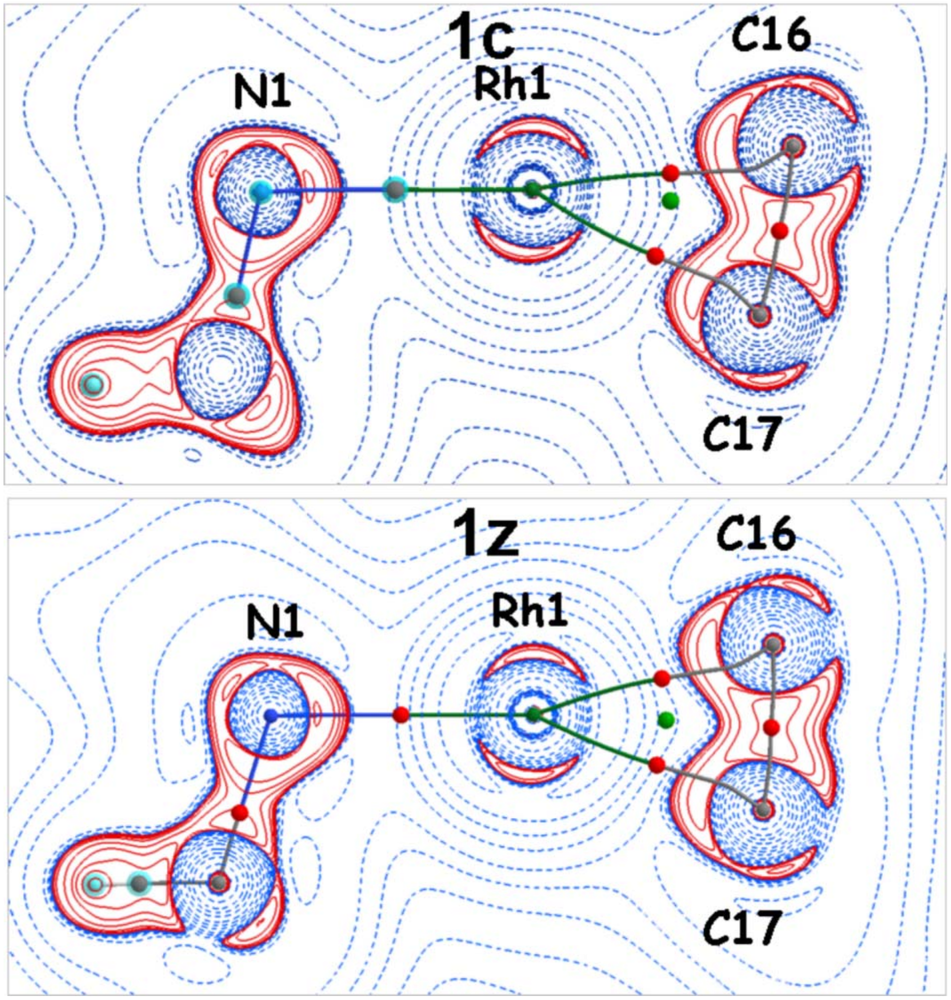

**Fig. 5**

Maps of the laplacian in the plane Rh1–C16–C17 obtained from the single-point "sp" calculation at the experimental geometry: Top **C**-sp, bottom **Z**-sp. Positive contours are solid red lines, negative contours as dashed blue lines. The lines linking the nuclear positions are the bond paths, atoms surrounded by a diffuse blue halo are slightly out of the plane of the figure. Only those bond paths trajectories that lie on the plane of the figure are plotted, those out of the plane are omitted. Red dots indicate the position of the bond critical points (BCP) and the green dots the location of the ring critical point (RCP).

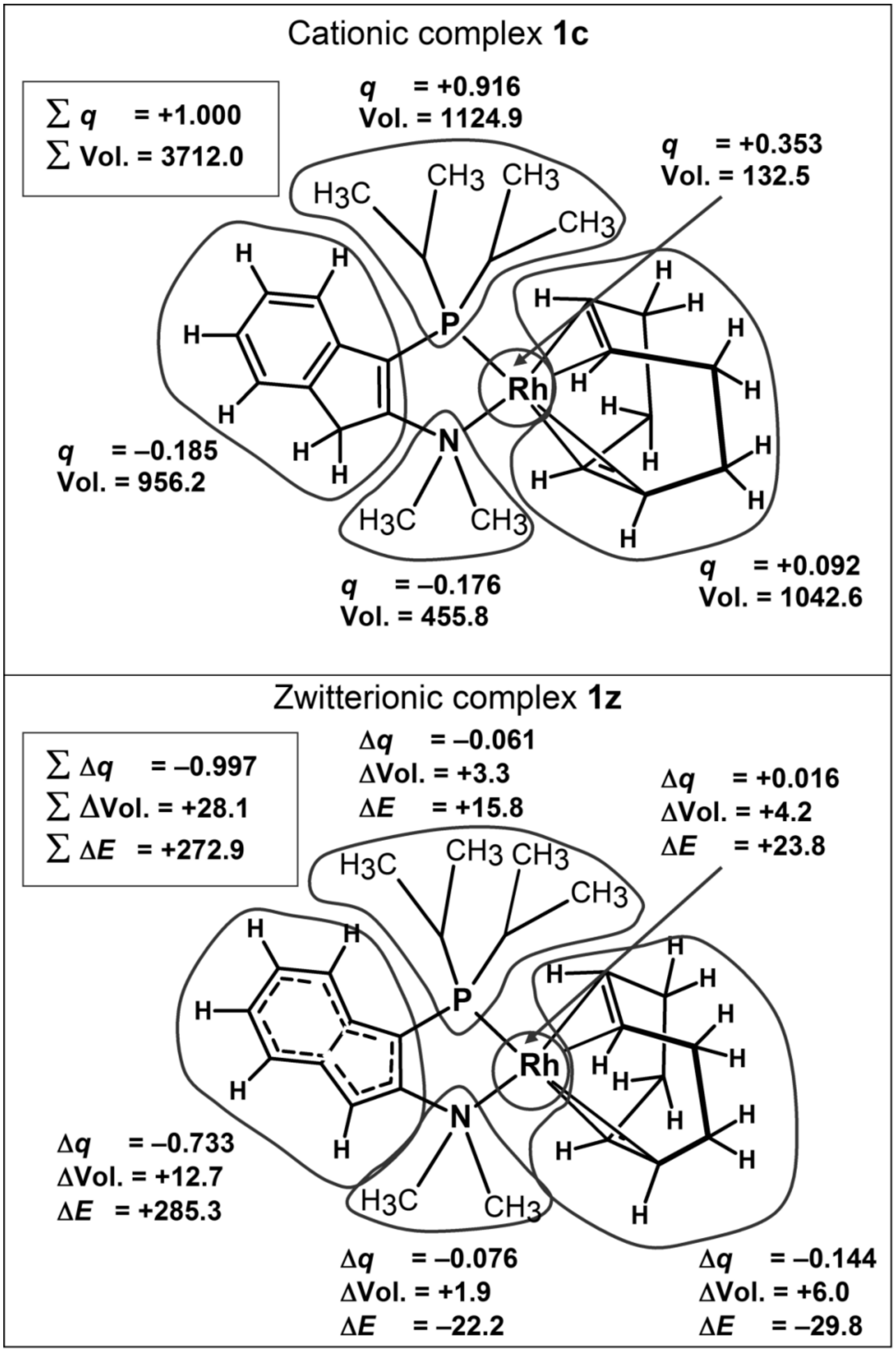

**Fig. 6**
Group properties (*P*) of complexes **1c** (top) and their changes ($\Delta P = P(\mathbf{1z}) - P(\mathbf{1c})$) in **1z** (bottom). Charges (*q*) and volumes (Vol) are given in atomic units and energies (*E*) in kcal/mol shown.

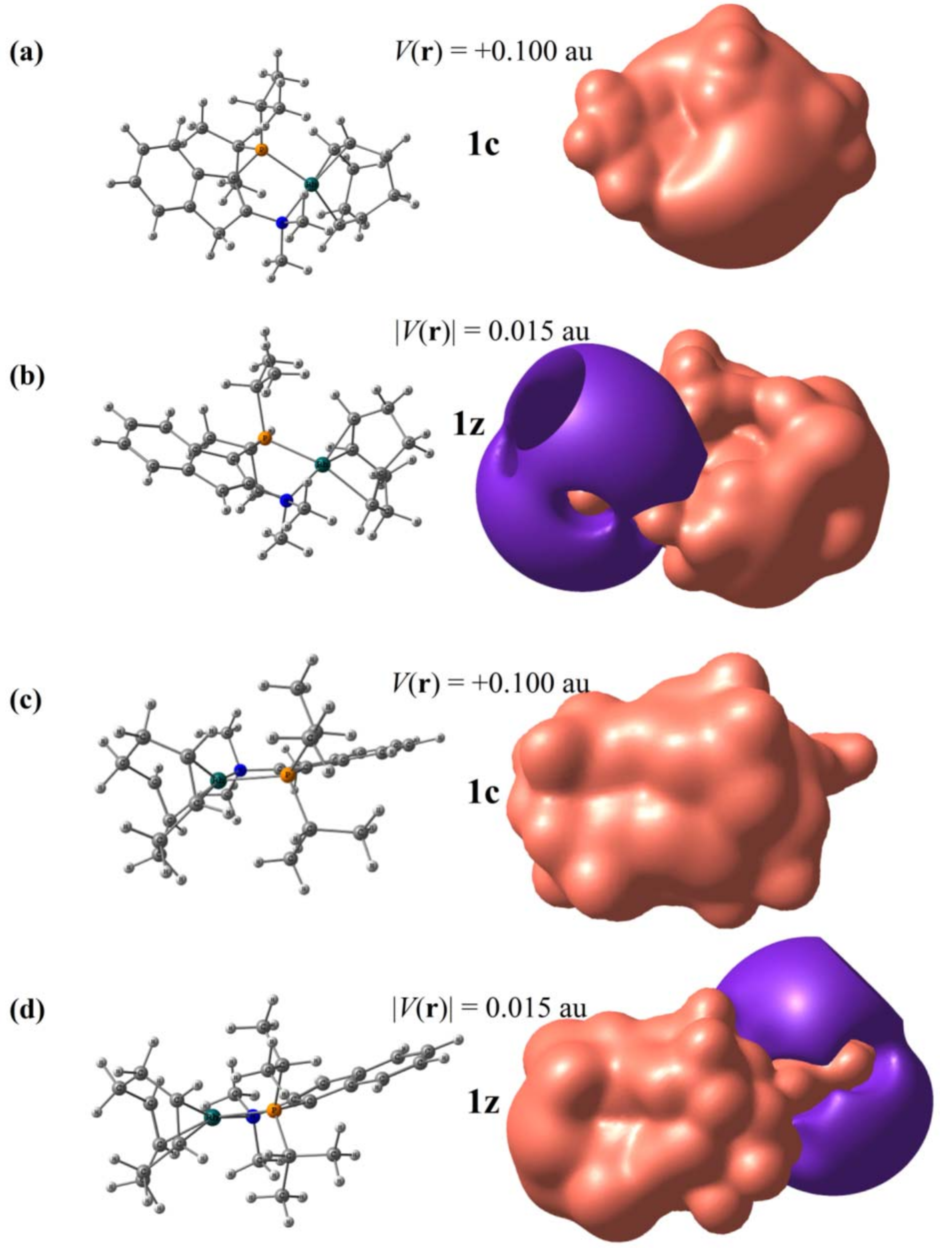

**Fig. 7**
Calculated molecular electrostatic potential (ESP) of the two complexes: Two isosurfaces (of magnitudes 0.100 and 0.015 au) showing that the similarity of form of the ESP around the two faces of the catalytic center carries to more than one value of the ESP. On the left is a representation of the molecular geometry in the orientation used to generate the corresponding potential on the right. Red = positive ESP, violet = negative ESP. **(a)** and **(b)** are orientation where the aromatic ring is on the left of the figure, whil;e **(c)** and **(d)** are rotated (roughly) by 180º to show the "back" of the molecule (the aromatic system is on the right of the figure).

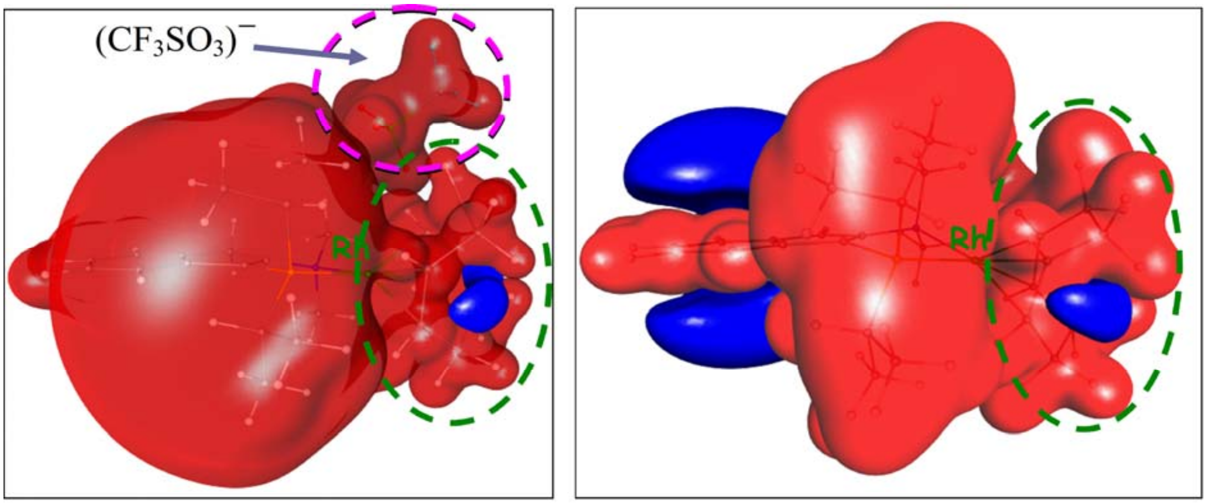

Cationic form (**1c**)
$(C_{25}H_{38}NPRh)^+(CF_3SO_3)^-$

Zwitterionic form (**1z**)
$C_{25}H_{37}NPRh$

**Fig. 8**
Experimentally-determined molecular electrostatic potential (ESP) at an isosurface with $|V(\mathbf{r})| = 0.05$ au that shows the similarity of the form of the ESP around the rhodium atom. (Red = positive ESP, blue = negative ESP).

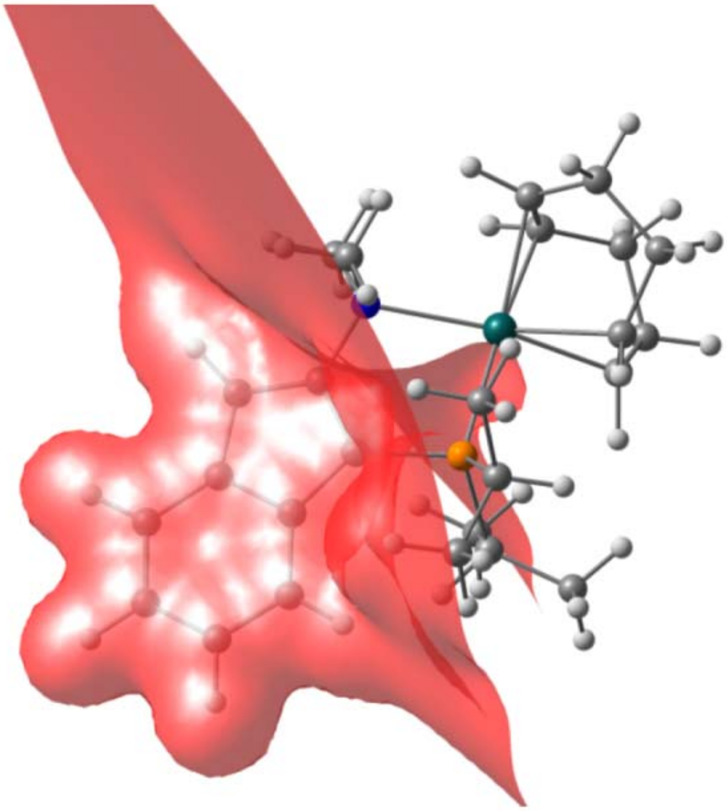

**Fig. 9**

Molecular electrostatic potential (ESP) nodal surfaces ($V(\mathbf{r}) = 0.000$ au) of the **1z** complex. The nodal surface partitions the complex into a region of negative ESP from the side of the aromatic system and a region of positive ESP surrounding the catalytic center that has a topography similar to that of this region in **1c**.

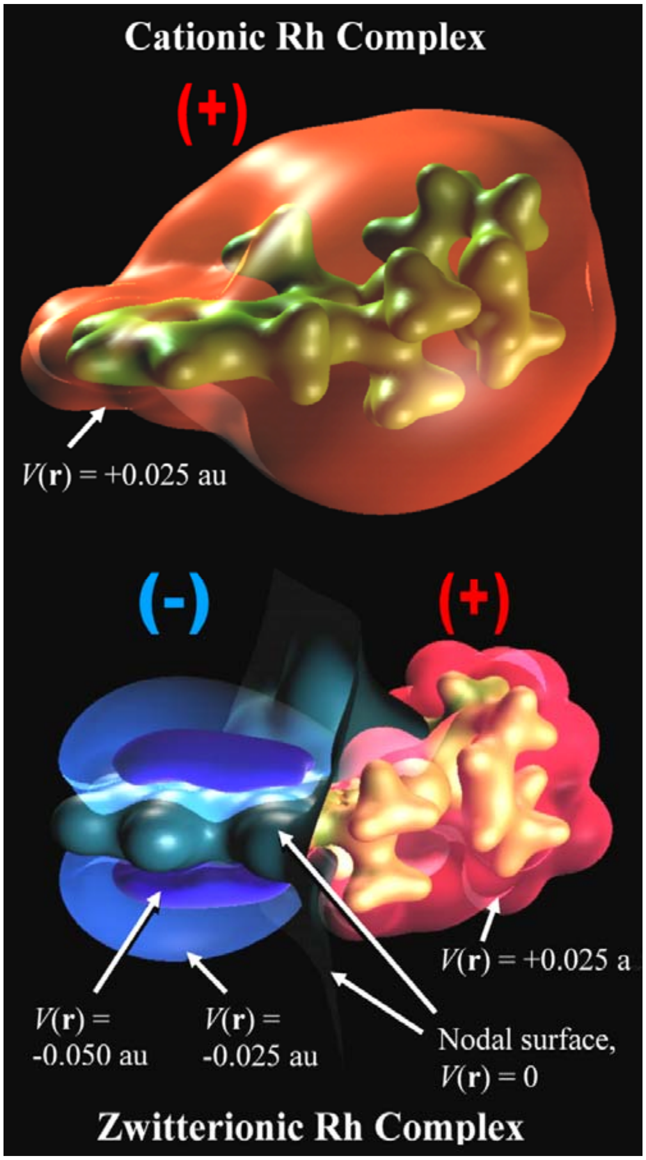

**Fig. 10**

Calculated molecular electrostatic potential (ESP), $V(\mathbf{r})$, in transparent envelopes, for a truncated model of **1c** (top) and **1z** (bottom) (truncated in that the ter-butyl groups attaced to the P atom are replaced by methyls). The red and blue envelopes represent positive and negative potentials, respectively, while darker surface (in **1z**) that surrounds the aromatic ring and splits the molecule into the aromatic side (left) and rhodium side (right) is the nodal surface separating the regions of positive and negative ESP. The inner solid golden surface isosurface of $\rho(\mathbf{r}) = 0.1$ au is a high electron density envelope in the region close to the nuclear framework of the complexes. The ESP of **1c** (top) is clearly positive everywhere (up to the chosen isosurface) with a depression near the aromatic ring. The ESP of **1z**, however, zwitterionic is partitioned by the nodal surface into teo contiguous regions of positive and negative values, the latter region exhibiting an increasingly more negative values the closer the isosurface is to aromatic ring (the inner dark envelope of $V(\mathbf{r}) = -0.05$ au).

# TOC Graphic and Synopsis

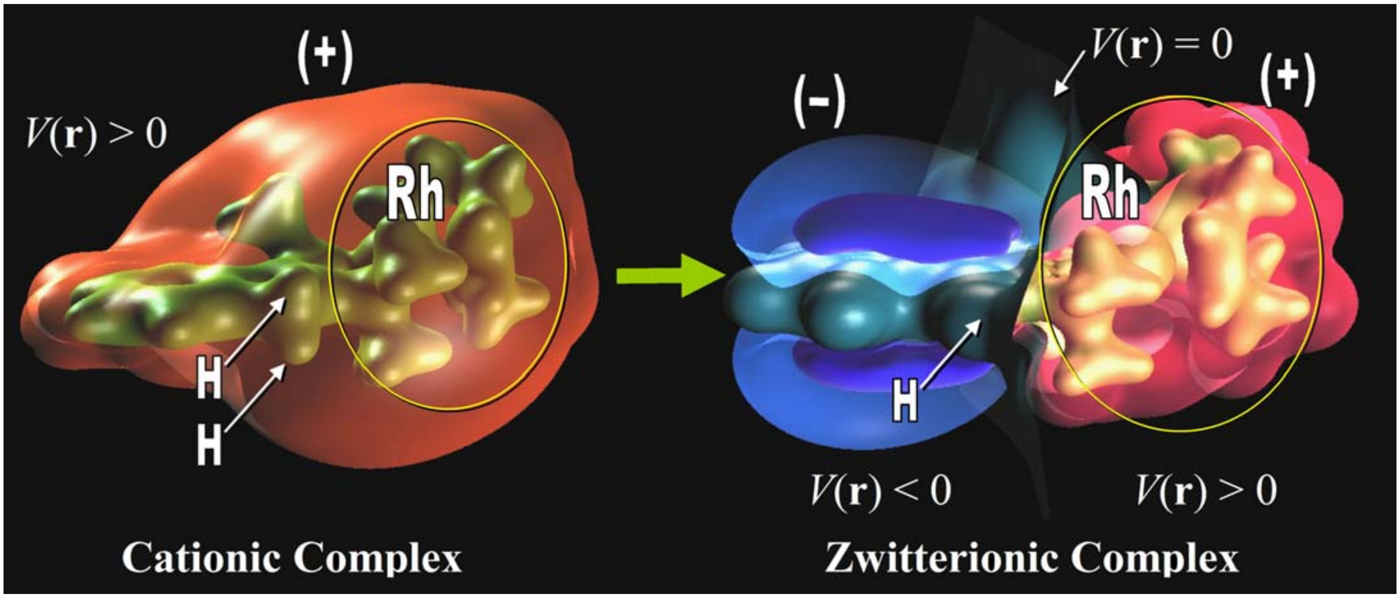

Low temperature synchrotron X-ray diffraction and high level of theoretical calculations were used to determine accurate electron density distributions of two structurally related cationic ([(κ$^2$-3-*P*$^i$Pr$_2$-2-*N*Me$_2$-indene)Rh(COD)](CF$_3$SO$_3$), [**1c**](CF$_3$SO$_3$)), and formally zwitterionic ([(κ$^2$-3-*P*$^i$Pr$_2$-2-*N*Me$_2$-indenide)Rh(COD)], **1z**) complexes, (COD = η$^4$-1,5-cyclooctadiene). Both experiment and theory show a striking similarity of charge distribution and of the molecular electrostatic potential, *V*(**r**), in the region of the Rh catalytic center. These observations confirm, for the first time, that appropriately designed zwitterionic complexes can effectively emulate the charge distribution found within cationic platinum-group metal catalyst complexes, in keeping with recent catalytic investigations.